ABSTRACT

DEPARTMENT OF PHYSICS

NANAYAKKARA, THARANGA R. B.Sc. UNIVERSITY OF COLOMBO, 2011

ELECTRONIC PROPERTIES OF NITROPHENYL FUNCTIONALIZED GRAPHENE AND BORON NANOTUBES

Committee Chair: Xiao-Qian Wang, Ph.D.

Thesis dated July 2015

We have studied the electronic characteristics of covalently functionalized graphene by nitrophenol groups using first-principles density-functional theory calculations. The nitrophenyl functionalization leads to a band gap opening in graphene and transition from a semi-metallic to semiconducting state. The induced gap is shown to be attributed to the modification of the π-conjugation that depends on the configuration for a pair of monovalent adsorption. A detailed analysis reveals that this intriguing magnetism modulation by strain stems from the redistribution of spin-polarized electrons induced by local lattice distortions. A detailed analysis suggests a sensitive and effective way to tailor properties of graphene for future applications in nanoscale devices.

The quest for low-dimensional boron structures has been motivated by the potential applications of light-weight materials. Recently, a semi-metallic two-dimensional boron allotrope was predicted *via ab initio* evolutionary structure search,

which is markedly lower in energy than the planar structures composed of triangular motifs and hexagonal holes. The emergence of a Dirac cone in the band structure demonstrates an intriguing perspective for quasiplanar counterpart of graphene. We studied the corresponding single walled boron nanotubes derived from the quasiplanar boron structure. In particular, our results are identified to have a Dirac cone, as well. The buckling and coupling between the two sublattices not only enhance the stability, but also are key factors to the emergence of the Dirac cone.

ELECTRONIC PROPERTIES OF NITROPHENYL FUNCTIONALIZED GRAPHENE AND BORON NANOTUBES

A THESIS

SUBMITTED TO THE FACULTY OF CLARK ATLANTA UNIVERSITY

IN PARTIAL FULFILMENT OF THE REQUIREMENTS FOR

THE DEGREE OF MASTER OF PHYSICS

BY

THARANGA RANJAN NANAYAKKARA

DEPARTMENT OF PHYSICS

ATLANTA, GEORGIA

JULY 2015

ACKNOWLEDGMENTS

The work presented would not have been possible without the support and guidance of several people. First, I would like to express my greatest appreciation to my advisor, Dr. Xiao-Qian Wang, for his invaluable guidance, patience, motivation, enthusiasm, immense knowledge, and supervision throughout the tenure of my study. He is a great teacher who is sharing his knowledge with student. His guidance helped me in all the time of research and writing of this thesis.

I also acknowledge the support given by Dr. Ronald E. Mickens, Dr. Alfred Z. Msezane, Dr. Michael D. Williams, Dr. Zhifan Chen, Dr. Swaraj S. Tayal, and the academic staff of the Department of Physics in Clark Atlanta University, who helped me throughout various projects. I wish to thank my colleagues Asanga, Mihiri, Kelvin L. Suggs, and all the other members of the research group for their assistance, perception, and advice. The research project was supported in part by the National Science Foundation (Grant No DMR-0934142).

Last but not the least, I would like to thank my family members for supporting and loving me.

TABLE OF CONTENTS

CHAPTER

LIST OF FIGURES

LIST OF TABLES

LIST OF EQUATIONS

LIST OF ABBREVIATIONS

DFT	Density Functional Theory
LDA	Local Density Approximation
NFE	Nearly Free Electron
GGA	General Gradient Approximation
PBE	Perdew-Burke-Ernzerhof
RKKY	Ruderman-Kittel-Kasuya-Yosida
HOMO	Highest Occupied Molecular Orbital
LUMO	Lowest Unoccupied Molecular Orbital
VBM	Valence Band Maximum
CBM	Conduction Band Minimum
BNTs	Boron Nanotubes
CNTs	Carbon Nanotubes

CHAPTER 1

INTRODUCTION TO GRAPHENE

Carbon is nonmetallic, tetravalent, and has four electrons available to form covalent chemical bonds. Carbon is the basis of all organic chemistry. Carbon-based systems show a number of structures with a variety of interest properties, because of the flexibility of sp^2 and sp^3 bondings. Many interests of physical properties are related to the reduced dimensionality of these structures. Among systems with only carbon atoms, graphene a two-dimensional (2D) allotrope of carbon, plays an important role as the basis for the understanding of the sp^2 electronic properties (*1-4*). Graphene layer is one atomic thick and carbon atoms are packed in a regular sp^2 bonded atomic scale chicken wire (hexagonal) pattern, see Figure 1.1.

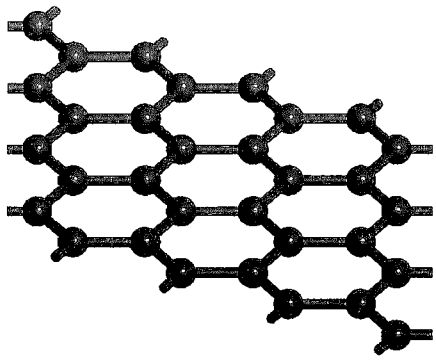

Figure 1.1. Honeycomb lattice structure of graphene.

A fullerene is a molecule composed of carbon in the form of a hollow sphere, ellipsoid and many other shapes. Spherical fullerenes are also called "buckyballs", and they are zero-dimensional objects with discrete energy states. Fullerenes can be obtained from graphene with the introduction of pentagons. Fullerenes can be viewed as wrapped-up graphene. Carbon nanotubes are cylindrical structures obtained by rolling graphene along a given direction and reconnecting the carbon bonds. Carbon nanotubes have only hexagons and can be thought of as one-dimensional (1D) objects (see Figure 1.2). Graphite is the most stable form of carbon under standard conditions. Graphite, a three-dimensional (3D) allotrope of carbon, was widely known after the invention of the pencil in 1564 (*1*). Graphite is made out of stacks of graphene layers that are weakly coupled by van der Waals forces.

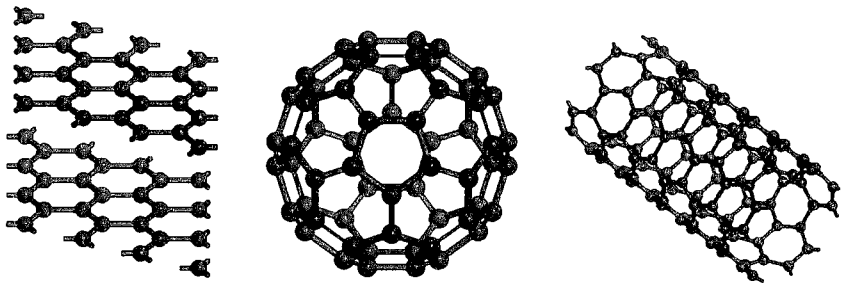

Figure 1.2. Perspective views of graphite (left panel), buckyball (middle panel), and nanotube (right panel).

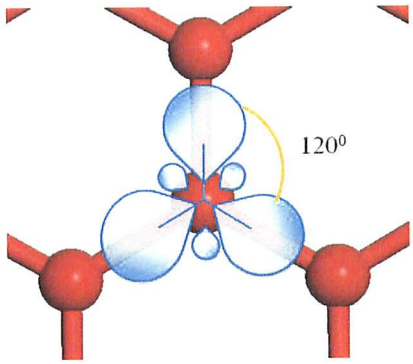

Figure 1.3. sp^2 hybridized orbitals in graphene layer.

For graphene, the mixing of 1s and 2p atomic orbitals creates the sp^2 hybridized orbitals. The sp^2 hybridization process involves the promotion of one electron in the 2s orbital to one of the 2p atomic orbitals. The set of formed hybrid orbitals creates trigonal structures. The angles between the hybridized sp^2 orbitals are 120° (see Figure 1.3). The sp^2 hybridized orbitals are the same in size and, energy. This sp^2 bond is about 1.42 Å (*1*).The unaffected p orbital, which is perpendicular to the planar structure, can bind covalently with neighboring carbon atoms, leading to the formation of a π band. Since each p orbital has one extra electron, the π band is half filled. The π electrons do not belong to a single bond or atom, but rather to a group of atoms. The extra electron in p orbital is responsible for the weak binding between the planes in graphene. The extra electron in p orbital is able to move around parallel and perpendicular to the graphene plane.

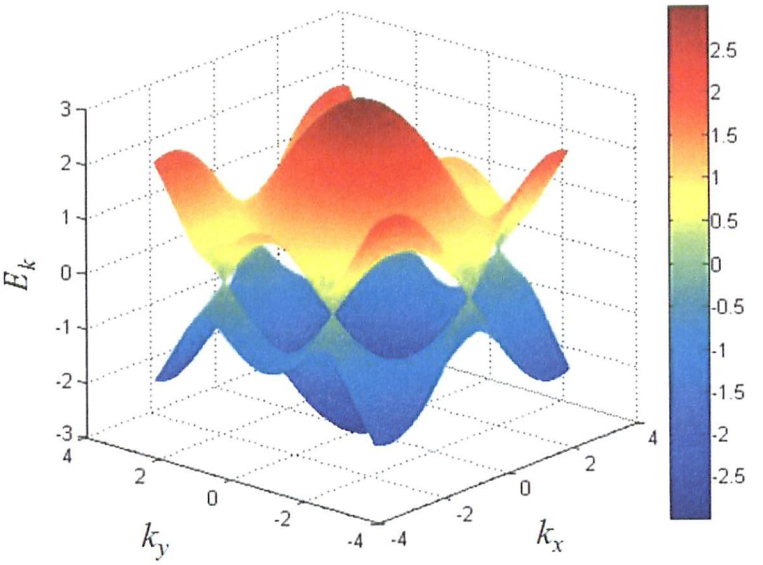

Figure 1.4. Calculated 3D-electronic band structures of honeycomb lattice of graphene.

Figure 1.4 shows the calculated band structure for graphene. Graphene is a semimetal with unusual linearly dispersing electronic excitations called Dirac electrons. Figure 1.5 illustrates the calculated valance band and conduction band of graphene. The upper half of the energy dispersion is called π^* or the conduction band. The lower half is called π or the valence band. The two bands are degenerate at the K and K′ points. The degenerated energy value is the energy of the Fermi energy of graphene. There are two atoms per unit cell in graphene. Since one atom contributes one π electron, there are two π electrons per unit cell. These electrons fully occupy the lower π-band, leaving the π^* antibonding band empty. The low energy excitations of graphene are massless chiral Dirac fermions. Dirac fermions behave in unusual ways as compared to ordinary

electrons, leading to new physical phenomena such as the anomalous integer quantum Hall effect measured experimentally (*80*).

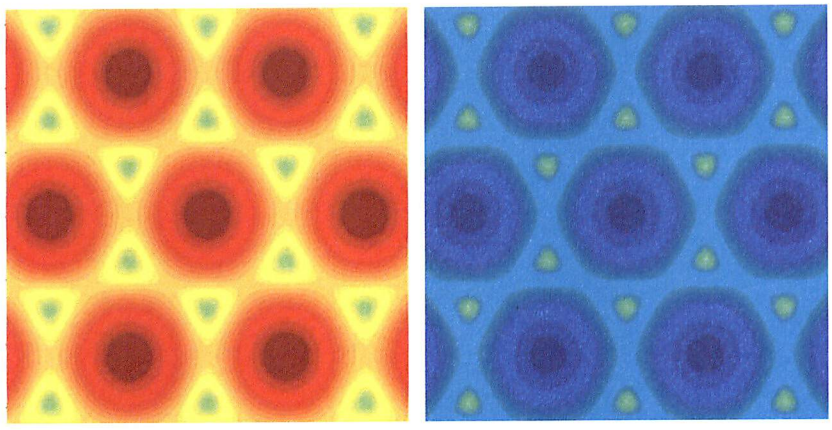

Figure 1.5. Calculated conduction bands and valance bands of graphene in the left and right panels, respectively.

Another interesting feature of Dirac fermions is that they can be transmitted through a classically forbidden region. The transmission phenomenon of Dirac fermions in graphene is known as Klein paradox. In fact, Dirac fermions behave in an unusual way in the presence of confining potentials. There has been a great deal of interest in trying to understand how disorder affects the physics of electrons in graphene and transport properties.

Graphene is unique in the sense that it shares properties of soft membranes, while it behaves in a metallic way. Graphene has out-of-plane vibrational modes that cannot be observed in 3D solids. The bending properties of graphene depend on flexural modes of the phonon band structure. Flexural modes are attributed to the lack of long range order in soft membranes, leading to the crumpling.

The unusual mesoscopic effect on graphene was investigated in early studies. The mesoscopic effect on graphene depends on the various types of edges in graphene. Zigzag and armchair edges have drastically different electronic properties. When coupled with conducting leads, the conductivity of graphene nanoribbons strongly depends on the edge structure of graphene nanoribbons. Quantum interference phenomena such as weak localization, the Aharonov-Bohm effect in graphene rings, and universal conductance fluctuations have been observed experimentally (*85*). The ballistic electronic propagation in graphene can be used to design the field effect devices such as *p-n* and *p-n-p* junctions. The Coulomb interactions are considerably enhanced in reduced geometries, such as graphene quantum dots, in which unusual Coulomb blockade effects and magnetic phenomena are observed (*86*). There are potential applications ranging from single molecule detection to spin injection.

Graphene can be tailored chemically and structurally in different ways due to the unusual structural and electronic flexibility. By controlling the properties of graphene layer, it is possible to create graphene based nonohybrids with novel magnetic and superconducting properties. Although the study of graphene is still in its infancy, the scientific and technological applications of graphene seem to be unlimited. Understanding and controlling the properties of graphene can open the doors for a new frontier in electronics.

CHAPTER 2

COMPUTATIONAL METHODS

2.1 Density Functional Theory

Density functional theory (DFT) is an approach for the description of ground state properties of metals, semiconductors, and insulators. The success of DFT not only encompasses standard bulk materials, but also complex materials such as proteins and carbon nanotubes. The main idea of DFT is to describe an interacting system of fermions via its density; not its many-body wave function. Under the one-electron approximation, the basic variable of the electronic system depends only on the spatial coordinates x, y, and z.

DFT has been applied to various fields such as geophysics, biomaterials, and nanomaterials. DFT has been used to investigate electronic structures, magnetic, and electric susceptibilities, and quantum Hall effects. Although DFT has been successful, there are some limitations of DFT, which include the lack of description of van der Waals interactions and band gaps being underestimated. The exchange-correlation potential is a functional derivative of the exchange correlation energy with respect to the local density. For a homogeneous electron gas, the local density approximation (LDA) only depends on the density of the electron gas. In inhomogeneous systems, the exchange correlation

depends not only on the local density, but also on nonlocal effects. In the LDA, the exchange-correlation potential is a function of the local density. The LDA can be used to predict electron densities, atomic positions, and vibration frequencies. DFT can provide robust predictions for the electronic structure of various material systems and verify experimental results.

The entire field of density functional theory rests on two fundamental mathematical theorems proved by Kohn and Hohenberg and the derivation of a set of equations by Kohn and Shami in the mid-1960s. The first theorem is that the ground-state energy from Schrödinger's equation is a unique functional of the electron density. The ground state energy E can be expressed as $E[n(r)]$, where the $n(r)$ is the electron density. The second theorem states that the electron density that minimizes the energy of the overall functional is the true electron density corresponding to the full solution of the Schrödinger equation.

A useful way to write down the functional described by the Hohenberg-Kohn theorem is in terms of the single-electron wave function, $\Psi_i(\mathrm{r})$. The energy functional can be written as,

$$E[\{\Psi_i(\mathrm{r})\}] = E_{known}[\{\Psi_i(\mathrm{r})\}] + E_{XC}[\{\Psi_i(\mathrm{r})\}] \tag{2.1}$$

The E_{known} term includes four contributions:

$$E_{known}[\{\Psi_i(\mathrm{r})\}] = \frac{h^2}{m}\sum_i \int \Psi_i^* \nabla^2 \Psi_i d^3r + \int V(r)n(r)\, d^3r +$$

$$\frac{e^2}{2}\iint \frac{n(r)n(r')}{|r-r'|} d^3r d^3r' + E_{ion} \tag{2.2}$$

In equation (2.2), on the right are, in order, the electron kinetic energies, the Coulomb interaction between the electrons and the nuclei, the Coulomb interaction between pairs of electrons, and the Coulomb interaction between pairs of nuclei.

Where, $E_{XC}[\{\Psi_i(\mathrm{r})\}]$ -exchange-correlation functional

h -Plank constant

e -charge of the electron

m -mass of the electron

The Kohn-Sham equations have the form,

$$\left[\frac{h^2}{2m}\nabla^2 + V(r) + V_H(r) + V_{XC}(r)\right]\Psi_i(\mathrm{r}) = \varepsilon_i\Psi_i(\mathrm{r}) \tag{2.3}$$

On the left hand side of the equation (2.3), there are three potentials. The first potential $V(r)$ is defined as the interaction between electron and the collection of atomic nuclei. The second term $V_H(r)$ is called the Hartree potential and is defined by,

$$V_H(r) = e^2\int\frac{n(r')}{|r-r'|}d^3r \tag{2.4}$$

$V_{XC}(r)$ can be defined as a functional derivative of the exchange-correlation energy:

$$V_{XC}(r) = \frac{\delta E_{XC}(r)}{\delta n(r)} \tag{2.5}$$

2.2 Material Studio

Materials Studio is a commercial modeling and simulation software designed to allow researchers in materials science and chemistry to predict and understand the relationship of material's atomic and molecular structure with its properties and behavior.

2.3 DMol3 Module

DMol3 is a first-principles (*ab initio*) quantum chemistry software package that performs accurate theoretical calculations on a wide range of compounds, including metal clusters, biological compounds, organometallics, and organic compounds. DMol3 performs self-consistent solutions to the DFT equations expressed in a numerical atomic orbital basis. The solutions to the Kohn-Sham equations provide the wave functions and electron densities, which can be used to evaluate energetics, electronic, and magnetic properties of the system. DMol3 provides a reliable predictive method for theoretically exploring the properties of unknown compounds, as well as for explaining, on a microscopic scale, the properties of existing compounds. The relatively low computational requirements of the method allow the study of larger systems than would be possible with other *ab initio* methods.

CHAPTER 3

ELECTRONIC PROPERTIES OF NITROPHENYL FUNCTIONALIZED GRAPHENE

3.1 Introduction

Graphene, a single layer of graphite, is emerging as an extremely versatile material with remarkable properties and promising potential applications (*2-4*). The effective application of graphene transistors, integrated circuits, and biosensors requires improved nanoscale control of the structural and electronic properties of graphene. As graphene hosts a plethora of phenomena associated with the Dirac-like linear dispersion, it remains an interesting topic to investigate how the unusual single particle properties impact the physics of adatoms on graphene. Specifically, since conductivity cannot be turned on and off effectively, pristine graphene cannot be used as a transistor in logic applications, where high on/off ratios are required. Field-switching capabilities depend on the presence of a band gap in the electronic structure.

The key to graphene transistors is the control over the electronic properties as well as developing scale-up techniques on an industrial level. While mechanical exfoliation leads to very high sample quality, the yield of monolayer graphene is very low. Within the realm of single-layer graphene, electron confinement such that occurring when rolling up graphene into single walled nanotubes or cutting its edges to form

nanoribbons is the effective way to open a gap in the band structure. In this case, the translational symmetry is partially broken with the hybridization of two Dirac points. The result of opening a gap is inversely proportional to the confinement length. Alternatively, the production of epitaxial graphene by evaporation of surface layers of SiC requires rather restrictive temperature and time conditions. Reduction of graphene oxide derived by solution of graphite has also attracted considerable attention. A high degree of the reduction has been reached. However, the reduction of graphene oxide, to ideally clean graphene, is rather problematic due to a high energy of chemical binding of hydroxyl groups with graphene.

On the other hand, a wealth of approaches has been developed for non-covalently and covalently functionalized graphene (*10*, *15-17*). Developing chemical methods in order to tune material properties has become one of the most critical issues in the application of graphene technologies. Various chemical modification techniques have been shown not only enhance its solubilities and process abilities, but also render suitable properties for graphene based nanoelectronic and nanophotonic devices. The modification of graphene electronic properties has been carried out by well-established chemical functionalization techniques, in which groups such as H, OH, or F bind covalently to carbon atoms, transforming the trigonal sp^2 orbital to the tetragonal sp^3 state (*31*,*32*). Such transformations drastically modify the electronic properties.

Recent experimental studies have demonstrated an efficient method to covalently functionalize pristine graphene with the use of nitrophenyl group (*18*,*19*). In lieu of the

increasing amount of experimental and theoretical studies of chemically functionalized graphene, an improved understanding of how covalent functionalization impacts the morphology and electronic transport in graphene is pivotal for its future application in nanomagneto electronics/spintronics. During the past few years, extraordinary development has been achieved for carbon-based spintronics. A series of theoretical and experimental studies have been carried out to reveal the spin relaxation mechanisms and spin transport properties in carbon materials, mostly for graphene and carbon nanotubes.

Recent experimental results show that the nitrophenyl functionalized graphene has unprecedented magnetic properties even at room temperature. De Heer and co-workers have reported a comprehensive study of low temperature magneto transport, vibrating sample magnetometry and superconducting quantum interference measurement before and after radical functionalization. The scanning probe microscopy techniques were utilized to study the field dependent magneto electronic properties (*24*). The experimental results of de Heer reveal that nitrophenyl functionalized graphene can act as an organic molecular magnet with ferromagnetic and antiferromagnetic ordering that persists at temperatures above 400 K. The nitrophenyl orientation and degree of coverage directly affect the magnetic properties of graphene surface. The concentration of nitrophenyl functionalized graphene was found to be approximately five carbon atoms per nitrophenyl group. Aryl-radical functionalization of epitaxial graphene not only changes the electronic properties but, also leads to disordered magnetism in graphene sheet. The graphene sheet consists of a mixture of ferromagnetism (ferrimagnetism),

super paramagnetic, and antiferromagnetic regions (*24*). A radical chemical functionalization substantially increases the number of interacting unpaired local spins. Additionally, negative magnetoresistance implies the presentation of ferromagnetic coupling between neighboring atoms. Spins in relatively small 2D regions are aligned anti-ferromagnetically.

Haddon and co-workers reported experimental results of the effect of nitrophenyl functionalization on the magnetic properties of epitaxial graphene (*17*). They focused on the chemical functionalization of basal-plane graphene carbon atoms in order to control the electronic properties of epitaxial graphene (*18*). The transformation of the carbon centers from sp^2 to sp^3 introduces a barrier to electron flow by saturating the carbon atoms and opening a band gap that allows the generation of insulating and semiconducting regions in graphene wafers. The experimental results suggest that nitrophenyl functionalization induces magnetism in epitaxial graphene. The magnetism is confined to disordered clusters on the surface of the epitaxial graphene with magnetic anisotropy as a result of the distribution in the domain sizes, which gives rise to antiferromagnetic, ferromagnetic (ferrimagnetic), and superparamagnetic regions.

The formation of a covalent σ-bond to one of the basal plane graphene carbon atoms by attachment of a radical species generates a delocalized spin in graphene π-system. If subsequent functionalization takes place in the same sublattice, an open-shell structure results. The long-range couplings for magnetic ordering of the local moments

are expected to take place through spin alternation due to the presence of half-filled π-orbitals in graphene.

Nitrophenyl groups adopt random and inhomogeneous configurations on the graphene basal plane. The bonding of nitrophenyl groups with carbon atoms leads to slight elongation of graphene lattice spacing. Low levels of functionalization suppresse the electric conductivity of the resulting functionalized graphene, while highly functionalized graphene shows the opposite effect. This difference develops from the competition between the charge transfer and the scattering enhancement. Detailed electron transport measurements revealed that the nitrophenyl functionalization locally breaks the symmetry of graphene lattice. Nitrophenyl functionalization of graphene leads to an increase in the density of state near the Fermi level, thereby increasing the carrier density. On the other hand, the bonded nitrophenyl groups act as scattering centers, lowering the mean free path of the charge carriers and suppressing the carrier mobility.

Despite its importance, a systematic study of chemical functionalization for graphene is still lacking. Most importantly, there remains a paucity of investigations on how the electronic structure depends on the adsorption configuration of functional groups, which is pivotal for practical realization of electronic structure engineering. Another important issue concerns the electron mediated exchange interactions and the associated nearly free-electron states (NFE). NFE states are delocalized on the surface outside the atomic centers. When they are close to the band edge, NFE states become a determining factor of the band gap width.

Experimental advances have motivated our study of electronic structure characteristics of nitrophenyl functionalized graphene. Herein, we report on comprehensive results based on first-principles density-functional calculations. Nitrophenyl functionalized graphene perturbs the π-conjugation of graphene and the corresponding electronic properties change from metallic to semiconducting. We show that nitrophenyl functionalization leads to the band gap opening of graphene. Our work thus asserts the unique opportunity of tailoring the band gap of graphene with varying chemisorption composition.

3.2 Methodology

The structural and electronic properties were investigated using first-principles density-functional calculations. Our first-principles calculations are based on density functional theory as implemented in the DMol3 package. Perdew-Burke-Ernzerhof (PBE) parametrization of the generalized gradient approximation (GGA) was used in the calculations. A supercell with a vacuum space of 26 Å normal to graphene plane was used. A kinetic energy change of 2.0×10^{-5} eV in the orbital basis and appropriate Monchorst-Pack *k*-point grids of 4×4×1 were sufficient to converge the integration of the charge density. The optimization of atomic positions proceeds until the change in energy is less than 1.0×10^{-5} eV per cell. Although the GGA approach systematically underestimates the band gaps, we are primarily interested in the mechanism of gap

opening. The GGA approach is expected to provide qualitatively accurate information and remains the popular choice for investigations of covalent functionalizations.

In order to pursue the effect of addend concentration on the electronic structures, we have considered two configurations by adding one or two nitrophenyl groups onto a 5×5 rhombus cell, respectively. The cell constitutes 50 carbon atoms for graphene, 6 carbon, 2 oxygen, 1 nitrogen, and 4 hydrogen atoms for each nitrophenyl molecule.

3.3 Results and Discussion

In this work, we consider six different configurations for nitrophenyl functionalized graphene structures (see Figure 3.1). The binding energies were calculated for the geometrically optimized structures of the nitrophenyl functionalized graphene. Results are tabulated in Table 3.1.

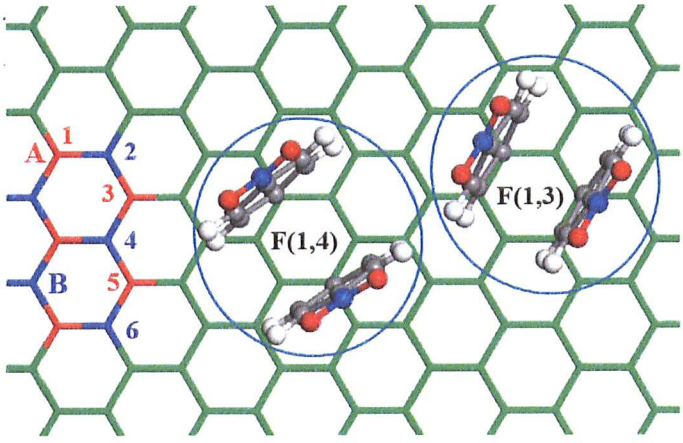

Figure. 3.1. Top view of the molecular structures of nitrophenyl functionalized graphene. Carbon, nitrogen, oxygen, and hydrogen atoms are colored in grey (green for graphene), light blue, red, and white respectively.

Addition of a single nitrophenyl group or a single carbon σ-radical to graphene leads to the formation of a delocalized spin in graphene π-system. If the second radical adds in a different sublattice, a spin paired antiferromagnetic structure results, whereas addition to the same sublattice gives ferromagnetic structure. The parallel alignment of the spins in a single sublattice favor to ferromagnetism because the spins are confined to the same sublattice.

Table 3.1. Calculated binding energies for six different configurations of the nitrophenyl functionalized graphene.

Structure	Spin Un-Polarized (eV)	Spin Polarized (eV)	ΔE (eV)
F(1,2)	-514.95032	-514.95148	0.00116
F(1,3)	-518.04560	-518.04561	0.00001
F(1,4)	-518.61631	-518.62479	0.00848
F(1,5)	-517.23089	-517.23130	0.00041
F(1,6)	-516.80819	-516.80902	0.00083
F(2, 5)	-516.65401	-516.65539	0.00138

The spin-polarized calculated results are lower in energy when compared with the corresponding spin-unpolarized results. The spin-polarized structures are energetically more favorable than spin-unpolarized structures. According to Table 3.1, F(1,3) and F(1,4) configurations are lower in energy among the six configurations of the nitrophenyl

functionalized graphene. Therefore, F(1,3) and F(1,4) were selected to study the electronic properties of nitrophenyl functionalized graphene.

We consider the simplest Kondo perturbation, where the radical is localized at a lattice site. There is theorem for the Ruderman-Kittel-Kasuya-Yosida (RKKY) interaction between these "site impurities" in bipartite lattices with hopping between opposite AB sublattices at half filling. The sign of the RKKY interaction depends only on whether the impurities are localized at opposite sublattices or on the same sublattices. The sign is dictated by particle-hole symmetry and is valid on all length scales. If nitrophenyl radicals are in AB lattice, the compound is antiferromagnetic. If nitrophenyl radicals are in AA lattice, the compound is ferromagnetic.

Figure 3.1 illustrates the optimized conformation of nitrophenyl functionalized graphene. The adduct increases the bond length linking to atoms on graphene. The corresponding bond length between the C atom on graphene and the C atom of the adduct nitrophenyl is around 1.59 Å for F(1,3) configuration and the corresponding value for F(1,4) configuration is 1.58 Å. The shortest distance between the nearest nitrophenyl neighbors on F(1,3) configuration is around 2.58 Å while that in the F(1,4) configuration is around 2.89 Å. The C-C bond lengths in graphene beyond the nearest neighbors are found to be little affected by the functionalization.

Graphene-addend interaction in the covalent functionalization has direct consequences on the electronic properties of graphene. Previous theoretical work investigated the addition of functional groups as free radicals to graphene (*31-33*). These

functional groups drastically disrupt the geometries and electronic structures of graphene by introducing local sp^3 hybridization, which induce a sp^3 type "impurity" state near the Fermi level (*14*,*35*,*36*). In the cases of divalent functionalization, two sp^3 states induced by two neighboring functional sites are shifted away from the Fermi level due to the rehybridization into bonding and antibonding states (*36*). Therefore, the local bonding configuration can significantly affect the electronic structure of functionalized graphene.

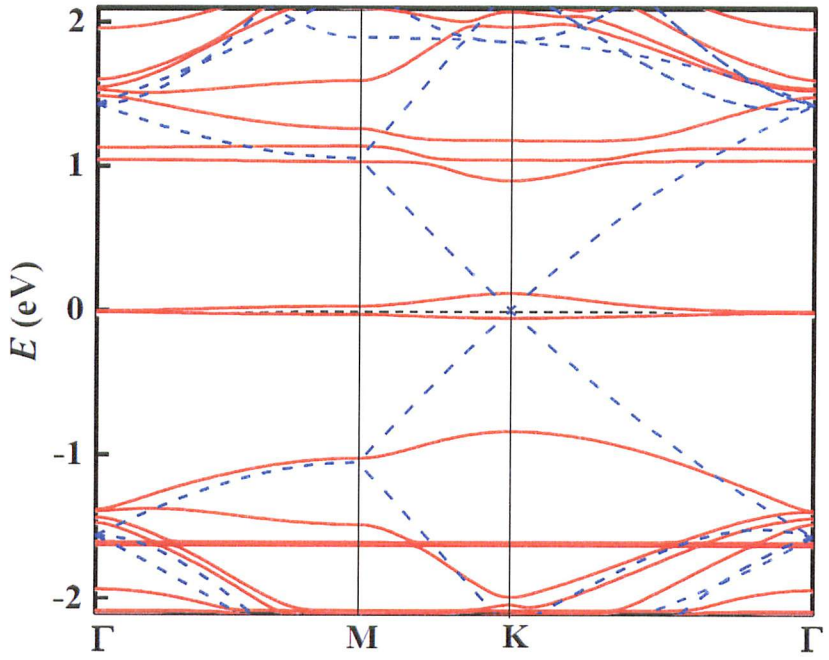

Figure 3.2. Calculated band (red color line) structures for nitrophenyl functionalized graphene F(1,3) configuration and pristine graphene (dashed blue line) respectively. $\Gamma = (0,0)$, $K = (\pi/3a, 2\pi/3a)$, $M = (0, \pi/2a)$, where $a = 12.3$ Å for a 5×5 rhombus unit cell. The Fermi level is shifted to 0 eV (dashed black line).

Figure 3.2 shows the calculated band structures for nitrophenyl functionalized graphene of F(1,3) configuration, along with the pristine graphene for comparison. One important feature of the band structure in the F(1,3) configuration is the semimetallic character of the system. The other characteristic is the presence of a flat band on the Fermi level in the spin up density, corresponding to a localized state on the connected nitrophenyl with graphene layer. The connected nitrophenyl, with graphene layer, is responsible for the total magnetic moment of the system. The nearest flat bands to the Fermi level are degenerate at the Γ point. Flat bands play an important role in the study of ferromagnetism.

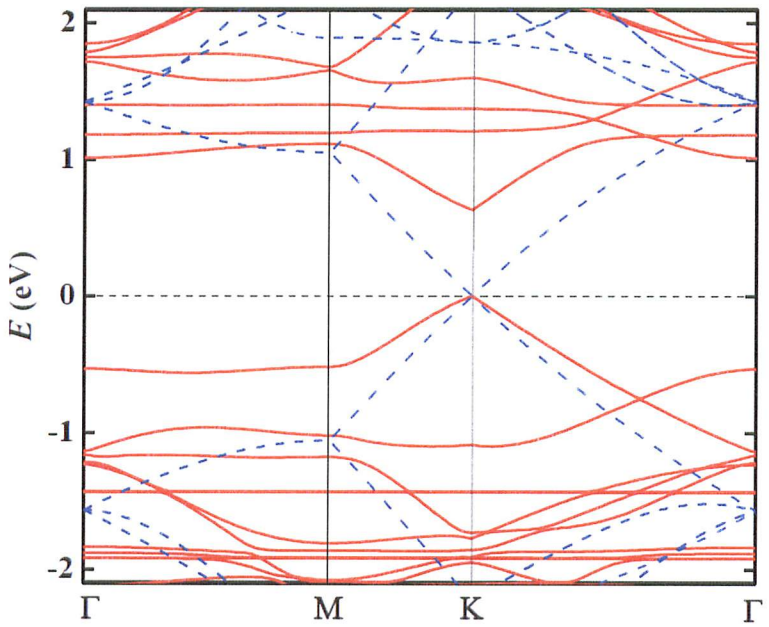

Figure 3.3. Calculated band (red color line) structures for nitrophenyl functionalized graphene F(1,4) configuration and pristine graphene (dashed blue line), respectively. Γ = (0,0), K = ($\pi/3a$, $2\pi/3a$), M = (0, $\pi/2a$), where a = 12.3 Å for a 5×5 rhombus unit cell. The Fermi level is shifted to 0 eV (dashed black line).

Figure 3.3 illustrates the calculated electronic band structure for the F(1,4) configuration of nitrophenyl functionalized graphene. There is a band gap opening at the K point. The extracted gap is approximately 0.62 eV. It is readily observable that after the covalent functionalization the π and π^* linear dispersion of pristine graphene in the proximity of the Dirac point (K) largely preserves, while a gap exists between the π and π^*states. These electronic properties of nitrophenyl functionalized graphene are in sharp contrast to the sp^3 rehybridization and loss of π electrons found upon addition of monovalent chemical groups in other functionalization schemes.

On the other hand, the present results are clearly distinctive to those of the noncovalent functionalization. For noncovalent functionalization, there is little modification of band structures close to the Fermi level, and the corresponding band structure constitutes flat and dispersed bands that can be readily classified as arising from functional group and pristine graphene contributions. By contrast, the nitrophenyl functionalized graphene displays profound level hybridizations. In particular, the band gap opening at the Dirac point implies important perturbations generated by the functionalization. All of the band gaps of the nitrophenyl functionalized graphene appear at the Dirac point. It is worth noting that although the C atoms on graphene connecting to nitrophenyl retain their sp^2 hybridization, the sp^2 hybridization angle is changed. As a result, the electronic structure of graphene is inevitably affected by nitrophenyl functionalization.

Closer scrutiny of the band alignments and dispersions near the Dirac point reveals that the gap opening is primarily attributed to the functionalization induced modifications of the π conjugation. The disruption of the original π conjugation is manifested in the level hybridization as seen in the band structure. Specifically, the highest occupied molecular orbital (HOMO) and the lowest unoccupied molecular level (LUMO) of nitrophenyl lieu up with the π and π^* bands of graphene. The band alignment is such that the interaction between flat and dispersed bands leads to hybridization-induced level avoided-crossing, which leads to the split of π and π^* bands of graphene into two hybridized bands each.

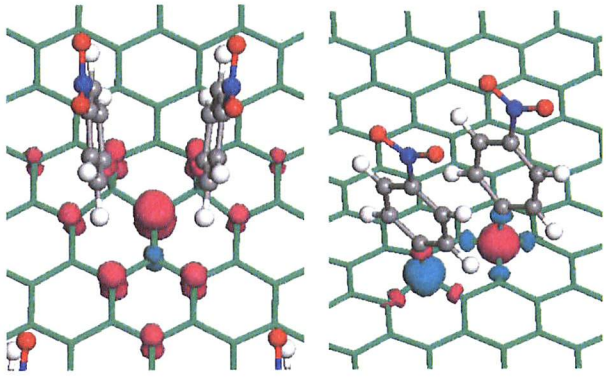

AA: Ferromagnetic *AB*: Anti-Ferromagnetic

Figure 3.4. Ball-and-stick presentation of optimized structures of nitrophenyl functionalized graphene with configuration F(1,3) and F(1,4) in left and right panel, respectively.

Figure 3.4 shows the charge densities of the corresponding hybrized bands at the band center (the Γ point). For those states, the charge density distributions display

predominant charge confinements on nitrophenyl addends for hybridized conduction and valence bands. This is to be contrasted to the conjugated π and π^* pattern on graphene. As can be seen in Figure 3.4, the increase of the addend concentration leads to proportional increase of the change of the π conjugation. This correlates with the associated increase of the band gap and thus provides support of the suggested scenario of the functionalization induced band gap opening. Careful examination of the charge density distributions also indicates the existence of σ and σ^* bonds in the hybridized states that attribute to the gap formation as well.

3.4 Conclusion

In summary, we have studied the electronic characteristics of nitrophenyl functionalized graphene. We have shown that the nitrophenyl addition to graphene layer preserves the sp^2 hybridization network of the carbons on graphene. However, the π conjugation of graphene near the Fermi level is greatly disturbed by functionalization, which leads to the opening of a band gap dependent upon the addend concentration. This contrasts with the free-radical functionalization case where a sp^3-type band is induced close to the Fermi level. Such dependence of the electronic properties on the degree of functionalization of graphene suggests a novel and controllable method for the "band engineering" of graphene. Our findings on the nature of nitrophenyl functionalization induced band gap provide useful guidelines for enabling flexibility and optimization of graphene-based nanodevices.

CHAPTER 4

INTRODUCTION TO BOROPHENE

The deficiency is what accounts for boron being a strong Lewis acid, in that it can accept protons (H^+ ions) in solution. As boron is an electron deficient element next to carbon; there is a great deal of interest in the quest of quasiplanar nanostructures. The quasiplanar boron structures have received revived attention associated with the discovery of graphene, a monolayer of all carbon atoms. The unique Dirac cone linear dispersion of graphene is poised to succeed silicon as next generation of electronics transistors. However, it is known that pristine graphene is semimetallic. Therefore, engineering a band gap in graphene has been the subject of a plethora of recent experimental and theoretical investigations. Boustani indicated the small-sized boron clusters tend to form quasi-planar structures (*42*, *43*), which were later confirmed experimentally for B_{10}^- - B_{36}^- clusters (*47-50*). In comparison with graphene, the hexagonal network of boron is electron deficient and is not stable against the triangular lattice by capping the hexagon with a boron atom. The resultant triangular motif, however, is electron abundant. To rectify the electron abundance, 10-15% hexagonal hole concentration is important (*51*).

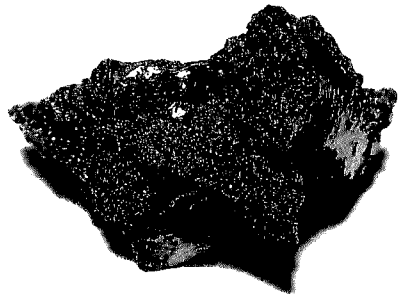

Figure 4.1. Boron appears as common mineral borax in the nature.

Recently, Zhou and co-workers uncovered a set of quasi-planar boron structures via *ab initio* evolutionary structure search (*77,78*). The predicted structures are markedly lower in energy than planar boron pseudoalloys (*51*). One of the lowest energy structures, referred to as *Pmmn* boron, was shown to have a linear dispersion Dirac cone, mimicking the band structure of graphene. The surface buckling is a common phenomenon for boron nanostructures. Considering the close resemblance to graphene, we refer the *Pmmn* boron structure to as borophene hereafter.

While the theoretically predicted quasi-planar structures are intriguing, the experimental realization of quasi-planar structures is yet to come. The challenges having the experimental works involve the lack of building blocks, the metallic behavior of the predicted periodic structures, and the difficulty to "merge" those building blocks. Recent theoretical studies have focused on the effect of substrate and finite thickness structures (*69,76,120*).

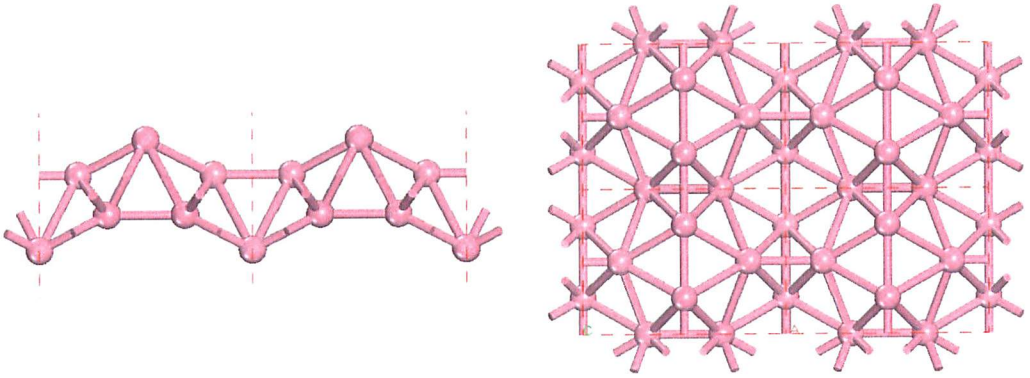

Figure 4.2. Side view (left) and top view (right) of borophene structure. Red color dash line represents the edge of the unit cell.

The borophene has eight atoms in a rectangular unit cell. In contrast to planar α-, β- and γ- boron sheets, there are no hexagonal holes in the borophene structure. Borophene contains triangles in the form of linking filled pentagons and filled hexagons. There are two straight lines of borophene, along with two buckled zigzag lines in a unit cell. Boron atoms on the straight and zigzag lines have six and seven bonds, respectively. It is worth mentioning that the other low energy conformation, borophene has two 7-bonded and six 6-bonded atoms in the unit cell, although it is metallic.

Two pentagons dovetailed each other and two hexagons are sharing two atoms on the edge. The bonds on the straight lines are linking the pentagons. The buckling of the structure is characterized by the "vertical" distance between the two straight lines, which amounts to ~1.5 Å. The bond length along the zigzag lines is 1.89 Å. Along the straight line, there are two distinguish bonds with lengths of 1.60 and 1.63 Å, respectively. The former is the bond linking two filled pentagons, while the latter is the one shared on two hexagons. This is attributed to the fact that the holes act as defects, which "traps" the

delocalized electrons. Remarkably, the 7-bonds building blocks have received a paucity of attention in recent years. It is worth noting that all quasi-planar pseudoalloys have bonds up to six.

Stable boron conformations can be constructed on the basis of two basic building blocks-the pentagonal pyramid B_6 and the hexagonal pyramid B_7, which is referred to as the "Aufbau principle" (*61*). The hexagonal B_7 is the precursor for convex and quasiplanar boron clusters and is thus closely connected to the α-boron sheet or boron nanotubes (*70,75,151*). The pentagonal B_6 unit is typically viewed as the building block of stable bulk boron. However, it is worth noting that the B_6 pyramid manifests itself as an aromatic component in planar boron clusters such as B_{19} (*117*). Heptagonal pyramid B_8 or the filled heptagon only exist in clusters. In practice, it is not feasible to have a planar structure with 7-bonds atoms. B_{80} boron fullerene contains empty twelve pentagons and towenty filled hexagons. By introducing B_6 into the boron fullerenes, we can reduce the energy of the fullerence.

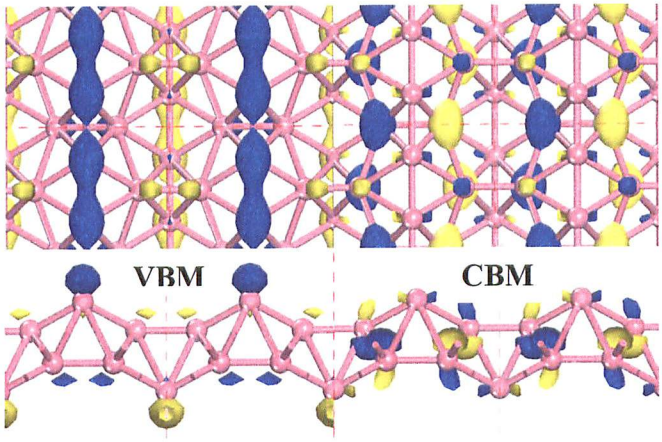

Figure 4.3. Extracted isosurfaces of valance band maximum (VBM) and conduction band minimum (CBM) for the borophene in left and right panels, respectively.

To investigate the electron distributions in borophene, we display in Figure 4.3 the extracted isosurfaces of the π and π * bands. As seen from Figure 4.3, the π electrons are primarily confirmed along the straight line with 6-bonded atoms, while the π * electrons are mainly located along the zigzag lines with 7-bonded atoms. The 7-bonded atoms have more delocalized electrons. The atomic positions on the straight lines of the borophene can be considered as the lattice A points. The atomic positions on the zigzag lines on borophene can be considered as the lattice B. According to the charge density distributions for the conduction band and valance band, the Dirac point has mirror symmetry along the x and y directions.

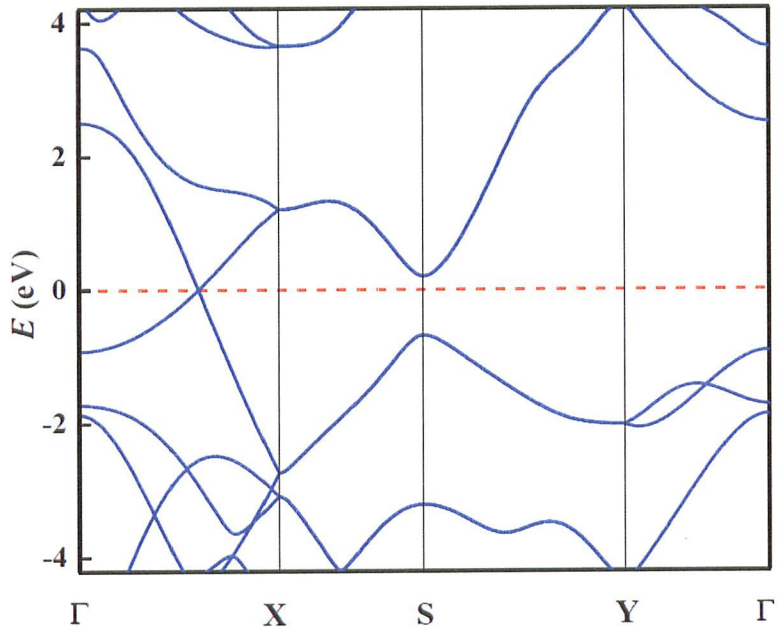

Figure 4.4. (Color line) Calculated band structure of borophene. First Brillouin zone Γ = (0, 0), X = (0, $\pi/2b$), S = ($-\pi/2a$, $\pi/2b$), and Y = ($-\pi/2a$, 0), where a = 4.52 Å and b = 3.26 Å. The Fermi level is shifted to 0 eV (dashed red line).

It is a standard practice in DFT to compute the exchange energy by one electron approximation that is specified by the local electron density and its derivatives. One of the most popular of these semilocal density approximations is the PBE model. Figure 4.4 displays the calculated band structures obtained from PBE. As seen from Figure 4.4, the PBE results indicate a semi-metallic and linear dispersion in the band structure of borophene.

The borophene structure is identified to have a Dirac cone (see Figure 4.4), the first in non-graphene-like 2D materials. The buckling and coupling between the two constituent sublattices are the key factors for the energetic stability and the emergence of the Dirac cone. The separated π and π^* confinements imply that the Dirac cone semi-metallic behavior is incidental. Longrange exchange can potential remove this accidental degeneracy.

CHAPTER 5

ELECTRONIC PROPERTIES OF BORON NANOTUBES

5.1 Introduction

Boron nanostructures are predicted to possess special properties superior to those of other nanomaterials. Boron nanotubes (BNTs) have been theoretically proposed to have metallic or semiconductors properties for armchair or zigzag ribbons. Since the synthesis of carbon nanotubes, efforts have been devoted to the synthesis of nanoscale tubular one dimensional structures with interest in their future application such as nanoscale electronic and optoelectronic. BNTs have attracted considerable interest in this regard. As compared with many non-carbon tubular materials, boron and boron based structures possess several unique properties: low densities, high melting point over 2300°C, excellent chemical stability, high thermal conductivity and high electric conducvity (*62*).

Most importantly, recent theoretical studies have shown that BNTs have tubular layer structure in contrast to carbon nanotubes (CNTs) (*45,151*). Theoretical calculation reveals that the BNTs possess metal-like density of states. The metallic behaviour may lead to interesting electrical and optical properties. BNTs may have high conductivity

that is independent of the chirality of the BNTs. This is in contrast to CNTs in which the conductivity depends on chirality of CNTs.

Based on experimental and theoretical studies, scientists predicted the existence of the single-walled BNTs. Experimentalist fabricated the BNTs in 2004 (*62*). Since then, many theoretical researches have been investigating single-walled BNTs. Single-walled BNTs are metallic. The double-walled BNTs based on buckle triangular sheet may be more stable than their single-walled BNTs. Buckling is closely related to the formation of interlayer bonds in double-walled BNTs (*151*). The study of BNTs is very important in light of experimental verification for the existence of boron nanotubular structures.

5.2 Methodology

Like CNTs, BNTs can be viewed as rolled up borophene two-dimensional sheet. We construct several BNTs by rolling up the 2-D borophene sheet as shown in Figure 5.1, following the same construction method for CNTs. The borophene sheet and the constructed BNTs are both buckled. The constructed BNTs are periodic and thus, allow one to calculate the band structures. The calculated band structures of the BNTs derived from borophene sheet have Dirac cone at the Fermi level. To our knowledge, there is no other BNTs reported in the literature that has Dirac cone. In addition, it may not be impossible to construct BNTs by rolling up only two unit cells of the borophene sheet. The BNTs with small diameters, derived from borophene, are missing the important properties such as the Dirac cone on the Fermi level. The distribution of the atoms in space is important for the characteristic of electronic band structure. The BNTs can be

started to construct by rolling up three unit cells of borophene structure around the *y* direction as shown in Figure 5.1. Unfortunately, the Dirac cone at the Fermi level was not observed for the BNTs with small diameters (< 6 Å). Interestingly, we can observe the Dirac cone at the Fermi level for BNTs with large diameters. In this research, the predicted BNT structures have buckled surfaces. Our results show that BNTs are semi metallic with zero densities of states around their Fermi energies. The stability of the BNTs depend on the diameter of the tube.

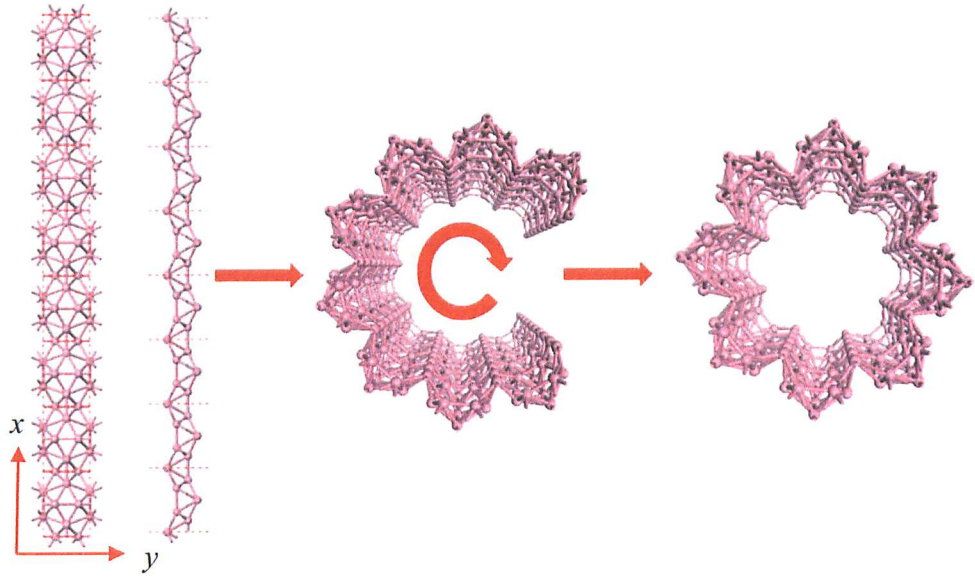

(a) (b) (c)

Figure 5.1. Constructed method of quasi-planer BNTs. (a) Top view and side view of borophene structure, respectively, (b) Intermediate step of the rolling up process and (c) Perspective view of constructed BNT (8,0) from borophene sheet.

We constructed one-prototype BNTs from the borophene sheet following the nomenclature of CNTs. The structural and electronic properties were investigated using first-principles density-functional calculations. Our first-principles calculations are based on DFT as implemented in the $DMol_3$ package. PBE parametrization of the GGA was used in the calculations. A kinetic energy change of 1.0×10^{-4} eV in the orbital basis and appropriate Monchorst-Pack *k*-point grids of $4\times1\times1$ were sufficient to converge the integration of the charge density. The optimization of atomic positions proceeds until the change in energy is less than 1.0×10^{-3} eV per cell. Although the GGA approach systematically underestimates the energy bands, we are primarily interested in the mechanism of Dirac cone at the Fermi level. Optimization of both the cell parameters and atomic positions were carried out by minimization of the total energy.

5.3 Results and Discussion

The important of this research work is that new kinds of BNTs were constructed by using borophene sheet. The novel BNTs have the Dirac cone at the Fermi level. Calculations were performed on these tubes with different diameters in the ranges approximately 4.5-17 Å, in order to explore their stabilities and electronic properties.

Table 5.1. Computed total energy (E_{total}), number of atoms in the unit cell (N), calculated binding energy ($E_{binding}$), and the radius of the BNTs from the borophene with respect to radius.

(m, n)	E_{total} (eV)	N	$E_{binding}$ (eV)	(Å)		
				r_{min}	r_{max}	$r_{average}$
(3,0)	-1840.3002	28	6.2517	1.50	3.00	2.25
(4,0)	-2457.7036	32	6.3099	2.49	4.24	3.36
(6,0)	-3683.4611	48	6.3131	3.24	5.50	4.37
(8,0)	-4914.9140	64	6.3698	4.56	6.85	5.71
(10,0)	-6146.1373	80	6.4010	6.02	8.13	7.08
(12,0)	-7377.0018	96	6.4181	7.47	9.67	8.57

The binding energies per atom of the considered BNTs are shown in Table 5.1. The binding energy is approaching to that of the borophene as the diameter increases. The large diameter has relatively high stability and stability increased with the increase of the diameter. All the calculated results indicate that the novel BNTs have metallic properties. Some selected typical structures and their corresponding electronic band structures will be discussed in next few pages.

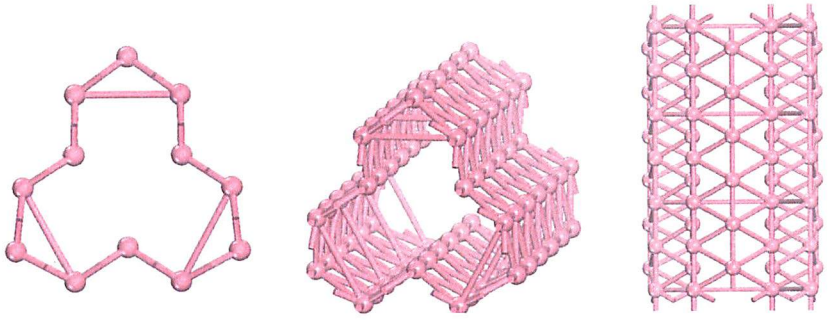

(a) (b) (c)

Figure 5.2. (a) Top, (b) perspective, and (c) side views of the geometric structure of BNT (3,0).

Figure 5.2 shows the BNT (3,0). The coordination numbers of the boron atoms on BNT (3,0) are 6 and 7. The band structure of the BNT (3,0) is shown Figure 5.3. The presence of significant charge density at the Fermi level indicates that the BNT (3,0) is metallic. For the band structure of the metallic boron nanotubes, there are several bands near the Fermi level, which ensure a large carrier density.

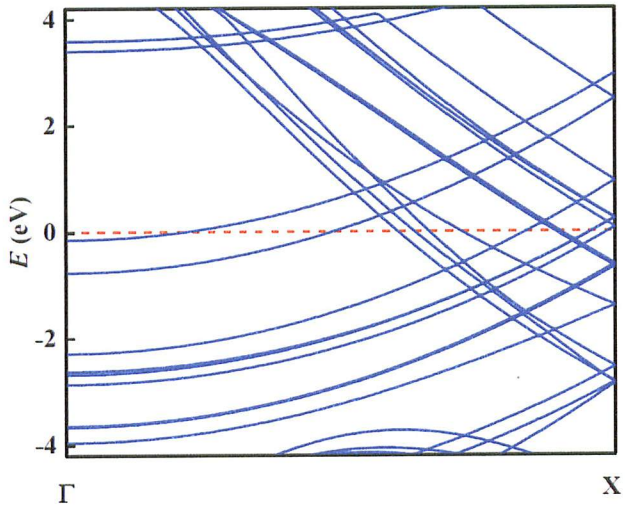

Figure 5.3. (Color line) Calculated band structures of BNT (3,0). Γ= (0, 0), X= (0, π/a), where a = 3.24 Å. The Fermi level is shifted to 0 eV (dashed red line).

These BNTs structures have surfaces composed of mixtures of pentagons, hexagons and triangles. It is important to note that these BNTs are deduced from borophene sheet do not have any holes; the hole density is zero.

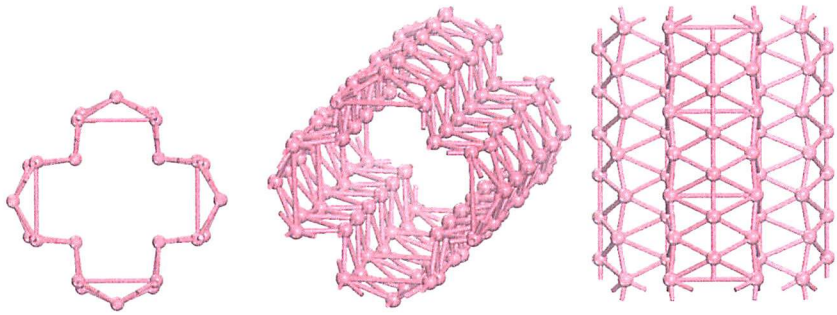

(a) (b) (c)

Figure 5.4. (a) Top view of the cross section of the BNT (4,0), (b) and (c) perspective, and side view of the optimized geometric structure of BNT (4,0), respectively.

Figure 5.4 shows the BNT (4,0). The coordination numbers of boron atoms on the BNT (4,0) are 6 and 7. The wall of the BNT (4,0) has eight number of linear chain atomic positions and eight number of zigzag chain atomic positions. There are hexagonal rings on the BNT (4,0) wall. These hexagonal rings consist of six corner atoms and one center atom. This may be explained by electron deficiency forcing the electrons to be shared at the surface. The center atoms serve as a bridge for electron transfer within the hexagonal rings. The calculated band structure for BNT (4,0) is depicted in Figure 5.5. The band decomposed charge density of BNT (4,0) is shown in Figure 5.6.

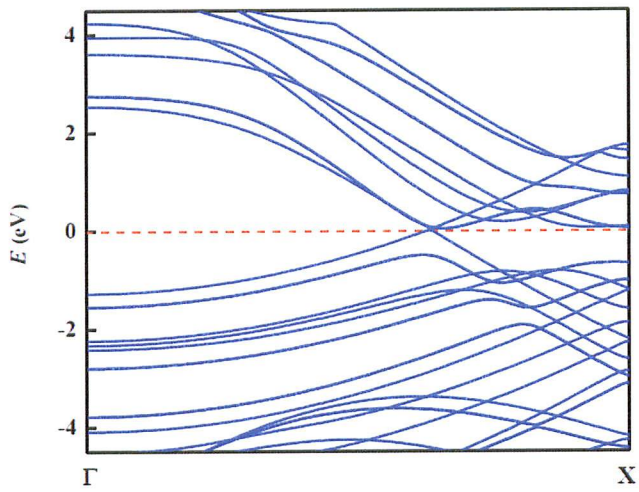

Figure 5.5. (Color line) Calculated band structures of BNT (4,0). Γ= (0, 0), X= (0, π/a), where a = 3.24 Å. The Fermi level is shifted to 0 eV (dashed red line).

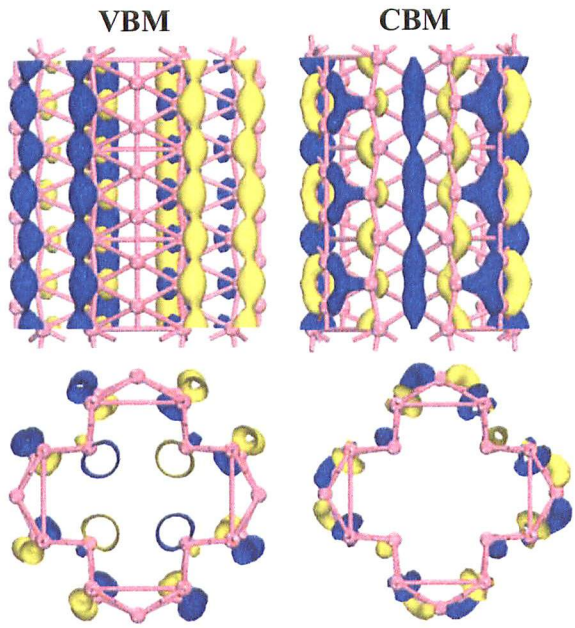

Figure 5.6. Extracted isosurfaces of valence band maximum (VBM) and conduction band minimum (CBM) for the BNT (4,0) in left and right panels, respectively. The components of the wave function are colored with blue and yellow, respectively.

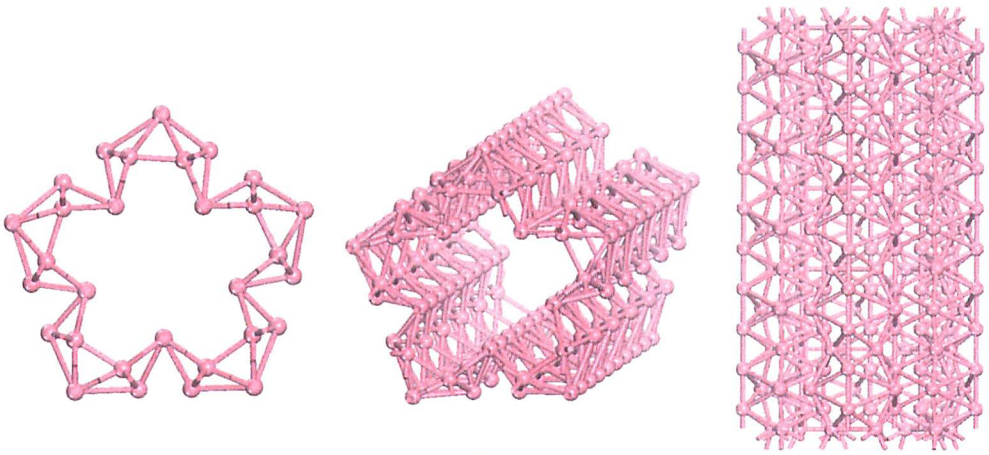

(a) (b) (c)

Figure 5.7. (a) Top view of the cross section of the BNT (5,0), (b) Perspective, and (c) side views of the geometric structure of BNT (5,0).

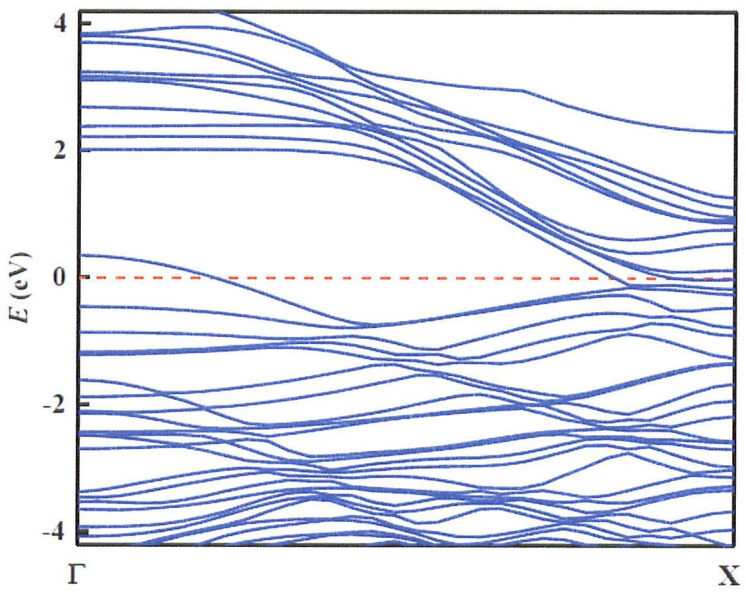

Figure 5.8. (Color line) Calculated band structures of BNT (5,0). Γ= (0, 0), X= (0, π/a), where a = 3.24Å. The Fermi level is shifted to 0 eV (dashed red line).

Interestingly, if Dirac cone lies slightly below the Fermi level, which means particular structure is self–doped and electrons are present as charge carriers. On the other hand, if Dirac cone lies slightly above the Fermi level that means particular structure is self–doped and holes are present as charge carriers.

In summary, the structural and electronic properties of novel boron nanotubes have been investigated at the DFT-GGA level. Within the scope of this research, the nanotubes rolled up from the borophene sheet are metallic independent of chirality. The predicted BNTs from this research have similar electronic properties, which may make them good candidates for fabrication.

Generally, 2D structures become more stable with increasing their thickness as they approach the bulk state. In addition, scientists believe that the buckling is driven by mixing of in plane sigma (σ) and out of plane pi (π) states. Further, once 2D structure becomes buckled, the original reflection symmetry may be lost. The thickness of this borophene structure is ~2.18 Å. The borophene is made of buckled triangular layers. The structure of borophene has two kinds of B-B bonds between two sub lattices with bond length of 1.80 Å and 1.89 Å, respectively. There are eight atoms in the unit cell of borophene structure. The structure of borophene contains straight lines and zigzag lines. There are seven bonds around the boron atoms, which are located on the zigzag line. Each boron atoms on the straight line has six bonds around them. This borophene structure can be constructed from hexagonal pyramidal subunits and pentagonal subunits. The pentagonal pyramids in borophene unit cell dovetail the out of plane apices atoms, which are located on the centers of the hexagonal pyramids each other by single bonds. In

addition, the hexagonal pyramids in the borophene structure dovetails the apices atoms, which are located on the centers of the pentagonal pyramids, each other by single bonds. This borophene structure can be considered a convex structure since it has the out of plane apices atoms. The shortest bond of the borophene structure is the bond between two atoms, which are located on the center of the hexagonal pyramids. The shortest bond length is 1.60 Å. The bond length between the two apices atoms, which are located in the same unit cell is 1.64 Å. The all the bonds which are connected on the zigzag line have the equal bond length and also those bonds are the longest bonds in the borophene structure.

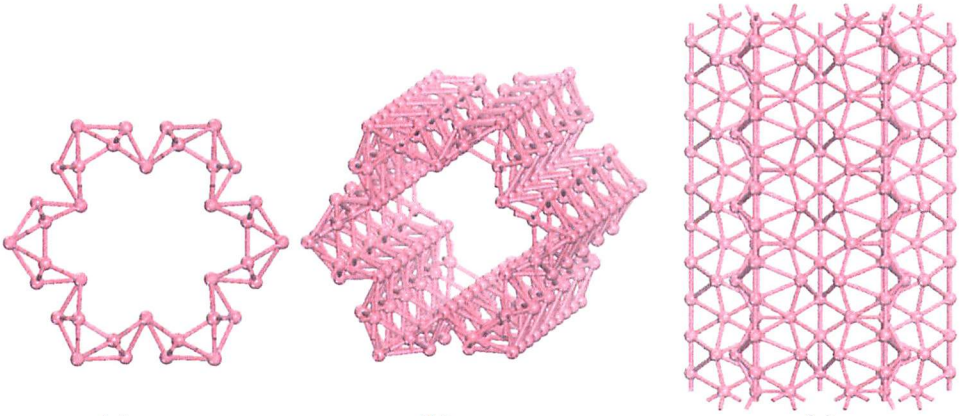

Figure 5.9. (a) Top view of the cross section of the BNT (6,0), (b) Perspective, and (c) side views of the geometric structure of BNT (6,0).

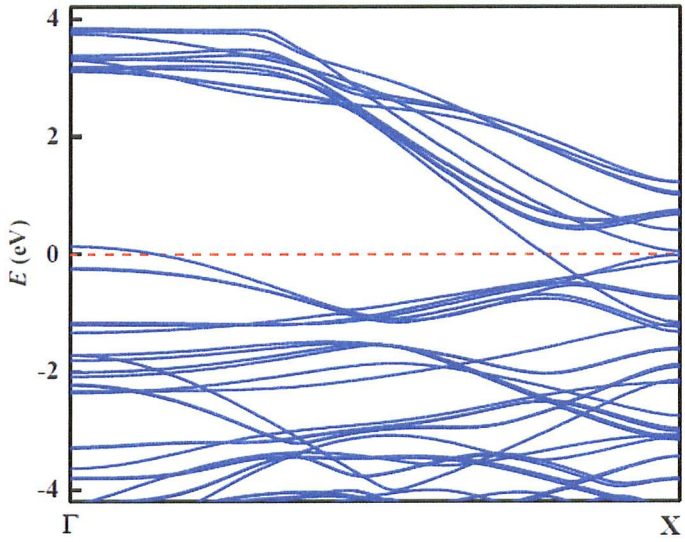

Figure 5.10. (Color line) Calculated band structures of BNT (6,0). Γ= (0, 0), X= (0, π/a), where a = 3.24 Å. The Fermi level is shifted to 0 eV (dashed red line).

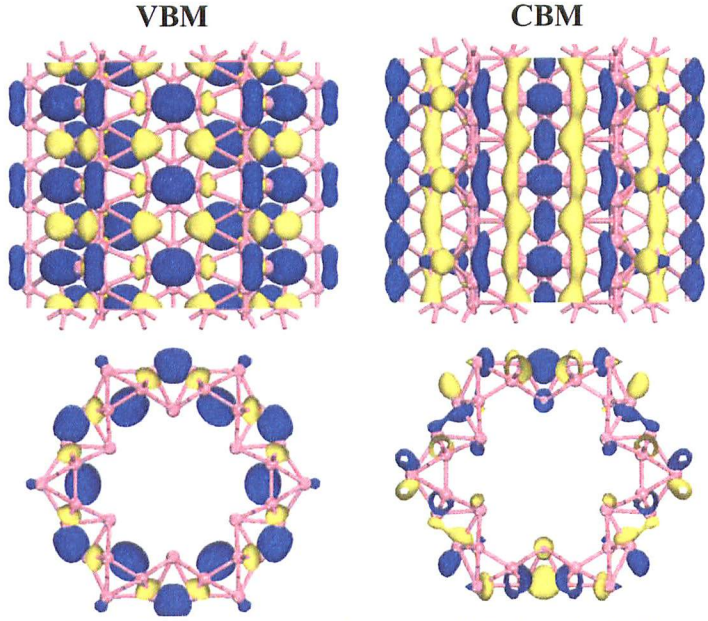

Figure 5.11. Extracted isosurfaces of VBM and CBM for the BNT (6,0) in left and right panels, respectively. The components of the wave function are colored with blue and yellow, respectively.

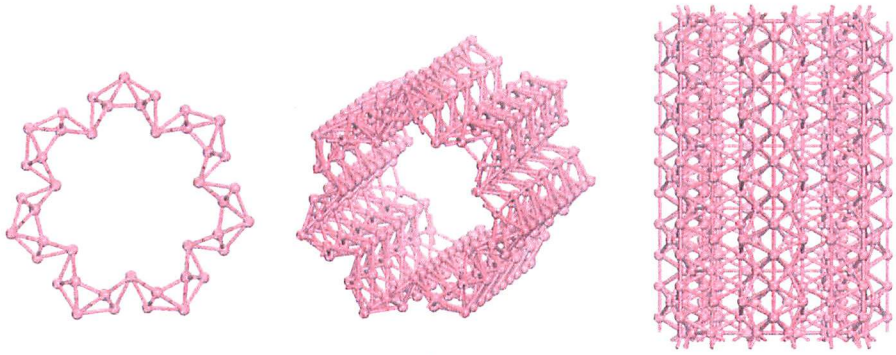

(a) (b) (c)

Figure 5.12. (a) Top view of the cross section of the BNT (7,0), (b) perspective, and (c) side views of the geometric structure of BNT (7,0).

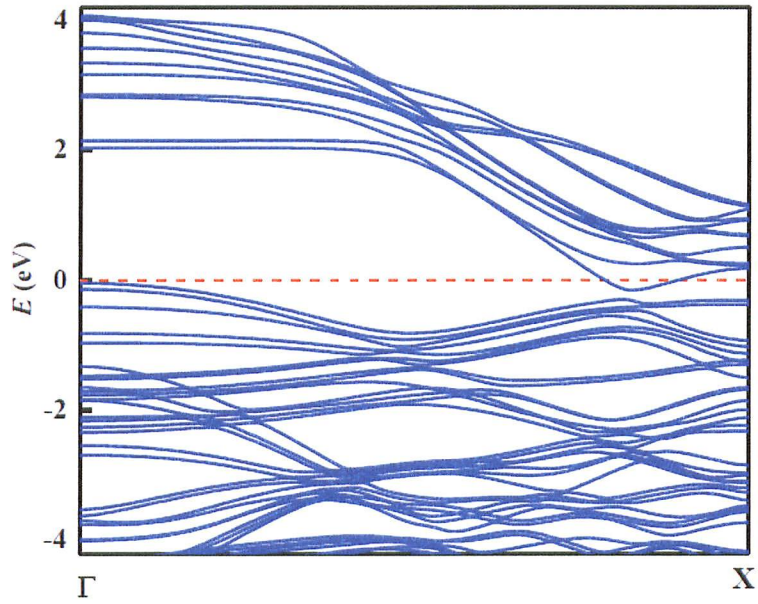

Figure 5.13. (Color line) Calculated band structures of BNT (7,0). Γ= (0, 0), X= (0, π/a), where a = 3.24 Å. The Fermi level is shifted to 0 eV (dashed red line).

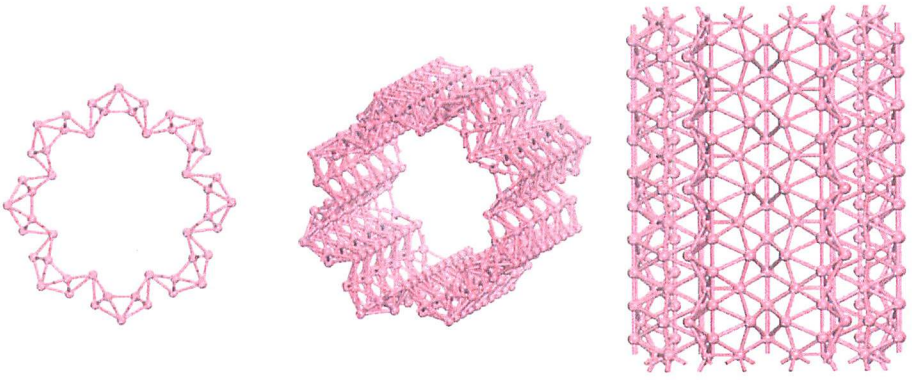

(a) (b) (c)

Figure 5.14. (a) Top view of the cross section of the BNT (8,0), (b) Perspective, and (c) side views of the geometric structure of BNT (8,0).

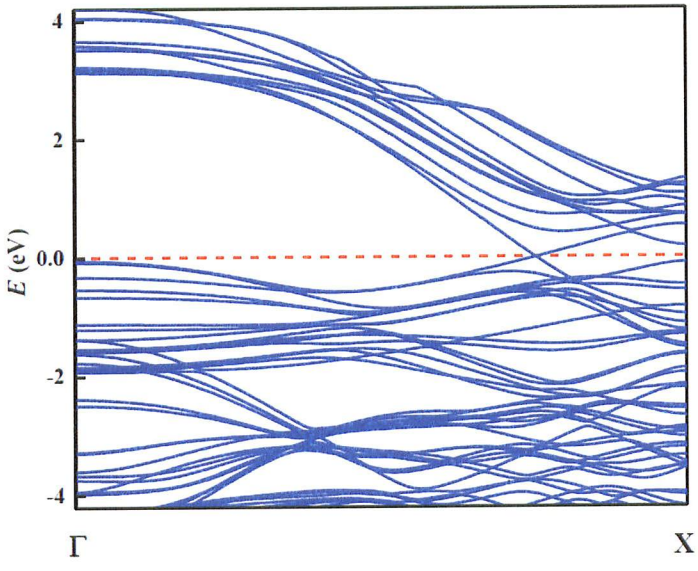

Figure 5.15. (Color line) Calculated band structures of BNT (8,0). Γ= (0, 0), X= (0, π/a), where a = 3.24 Å. The Fermi level is shifted to 0 eV (dashed red line).

Take the BNT (8,0) for example, the bands are degenerate near the X point and these bands are highly dispersive along the ΓX axis, imply that the effective mass of the charge carriers should be very small, and leading to high mobility and high conductivity. Hence, the BNTs could have potential as the metallic interconnects in the electronic devices.

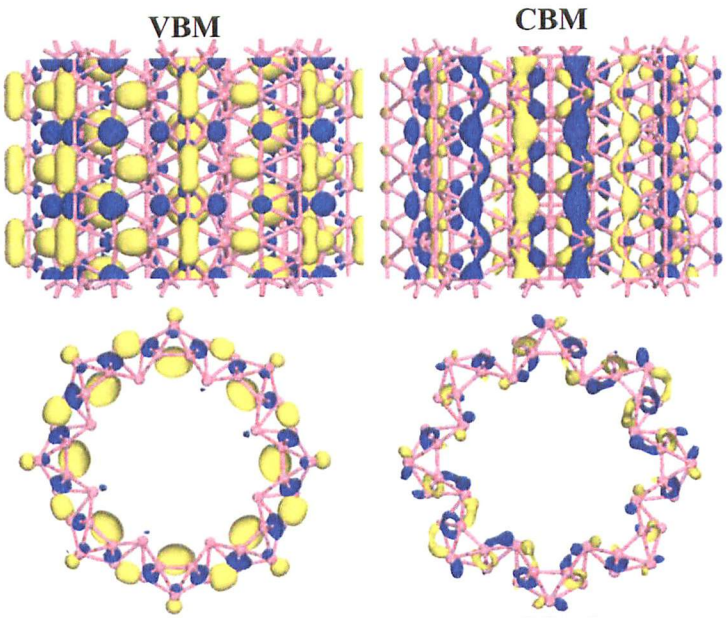

Figure 5.16. Extracted isosurfaces of VBM and CBM for the BNT (8,0) in left and right panels, respectively. The components of the wave function are colored with blue and yellow, respectively.

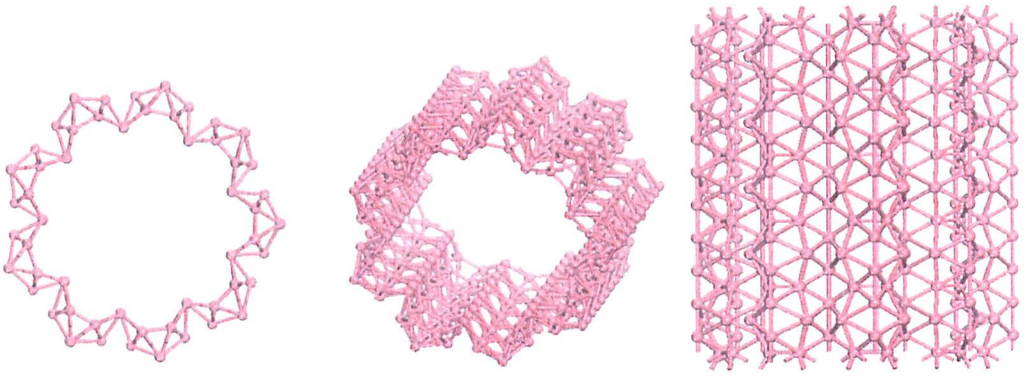

(a) (b) (c)

Figure 5.17. (a) Top view of the cross section of the BNT (9,0), (b) Perspective, and (c) side views of the geometric structure of BNT (9,0).

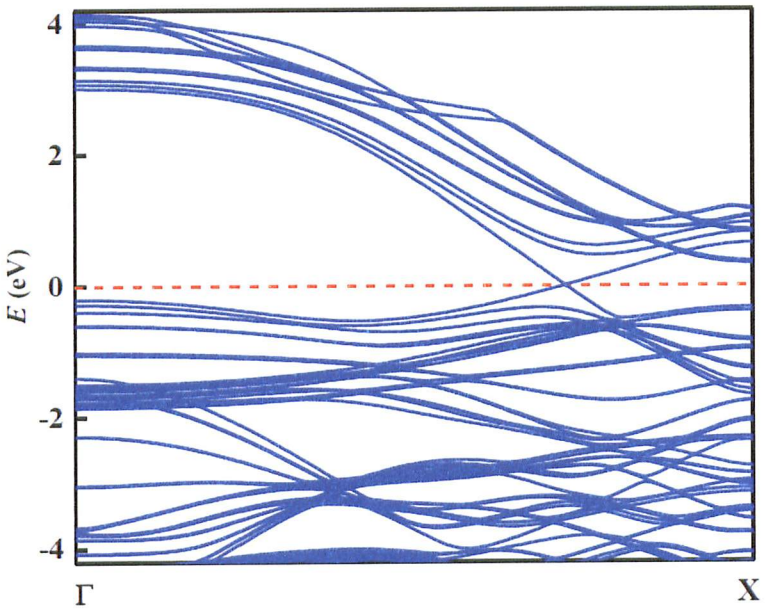

Figure 5.18. (Color line) Calculated band structures of BNT (9,0). Γ= (0, 0), X= (0, π/a), where a = 3.24 Å. The Fermi level is shifted to 0 eV (dashed red line).

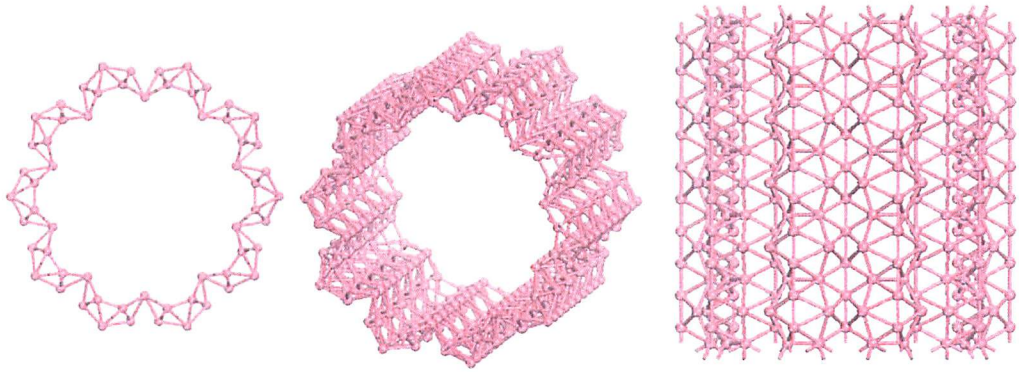

(a) (b) (c)

Figure 5.19. (a) Top view of the cross section of the BNT (10,0), (b) Perspective, and (c) side views of the geometric structure of BNT (10,0).

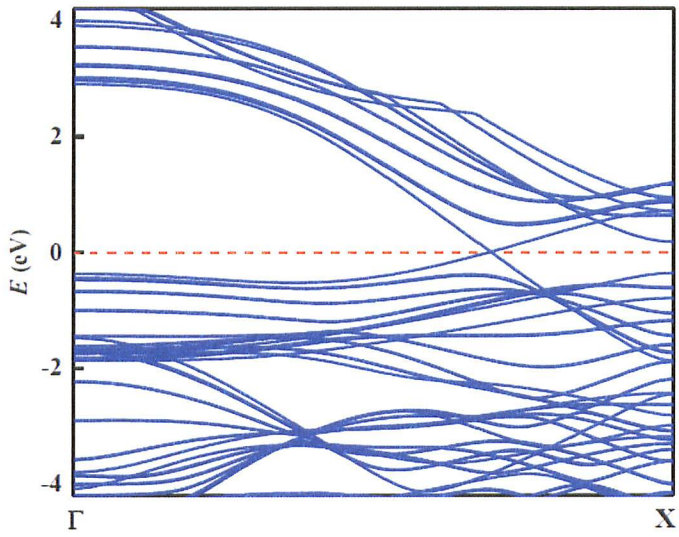

Figure 5.20. (Color line) Calculated band structures of BNT (10,0). Γ= (0, 0), X= (0, π/a), where a = 3.24 Å. The Fermi level is shifted to 0 eV (dashed red line).

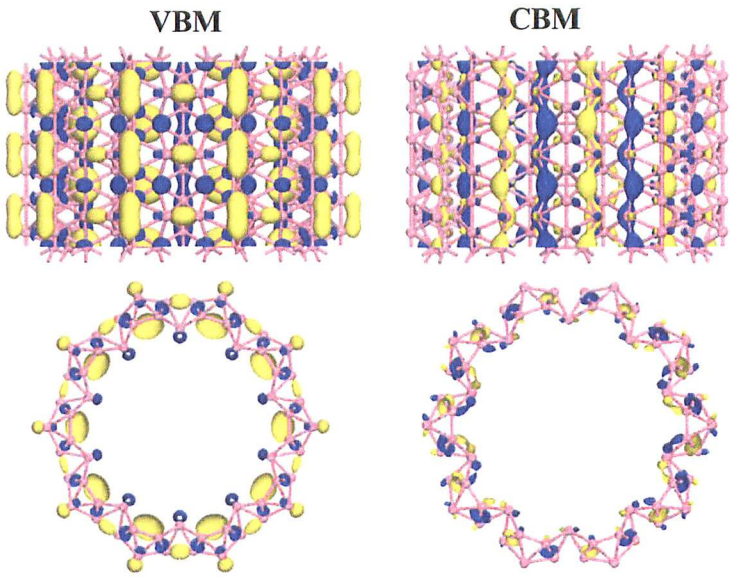

Figure 5.21. Extracted isosurfaces of VBM and CBM for the BNT (10,0) in left and right panels, respectively. The components of the wave function are colored with blue and yellow, respectively.

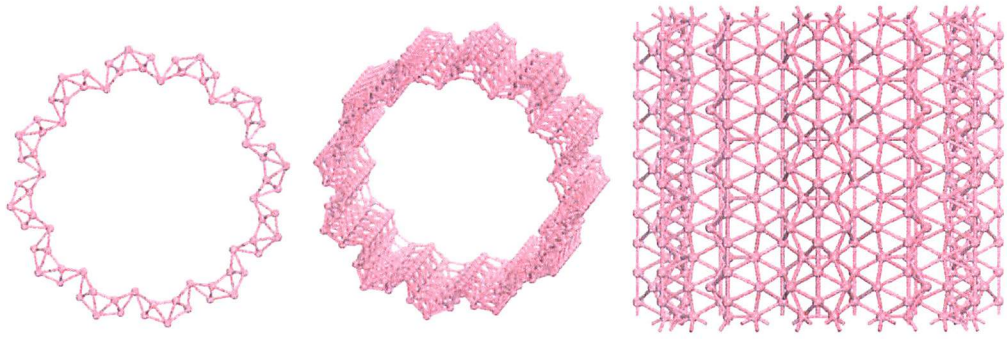

Figure 5.22. (a) Top view of the cross section of the BNT (12,0), (b) Perspective, and (c) side views of the geometric structure of BNT (12,0).

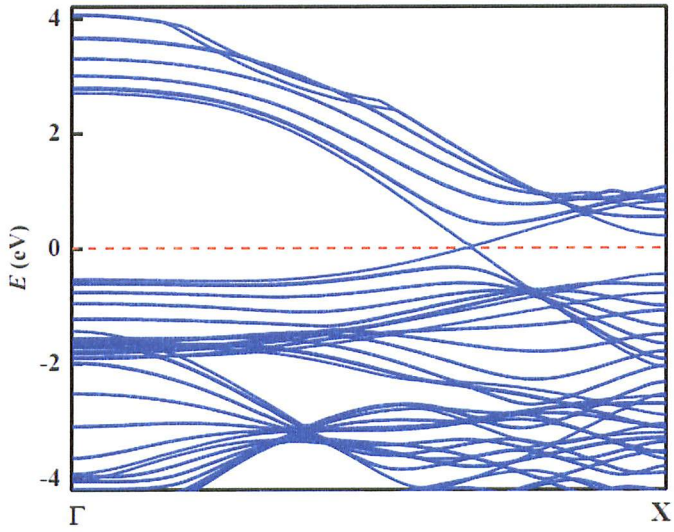

Figure 5.23. (Color line) Calculated band structures of BNT (12,0). Γ= (0, 0), X= (0, π/a), where a = 3.24 Å. The Fermi level is shifted to 0 eV (dashed red line).

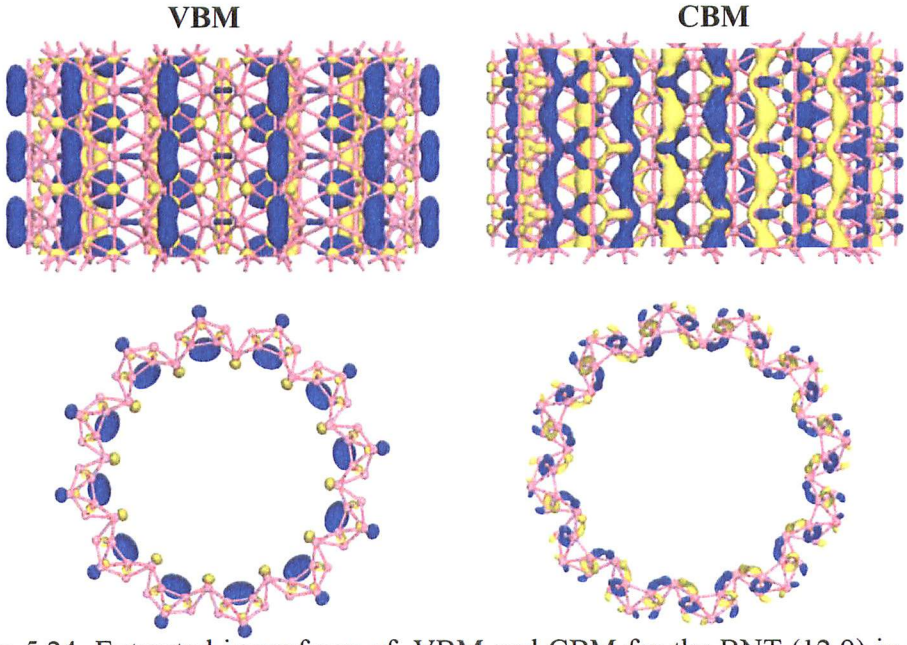

Figure 5.24. Extracted isosurfaces of VBM and CBM for the BNT (12,0) in left and right panels, respectively. The components of the wave function are colored with blue and yellow, respectively.

To understand the physical origin of the Dirac cone of the BNTs with large diameters, the band decomposed charge density at the Dirac point is plotted. The charge density distribution is extracted for the out-of-plane (p_z orbitals) states of two sublattices. The hybrids of in-plane states and out-of-plane states between two sublattices are responsible for the charge distribution of the lowest unoccupied molecular orbital (LUMO) in conduction band at the Dirac point. The charge density distribution for both the conduction and valence band at the Dirac point have mirror symmetry along the *x* and *y* directions. The hybrids of in-plane (p_x orbitals from the buckled boron chains) and out-of-plane states (p_z orbitals from the irregular boron hexagons) are a unique feature responsible for the emergence of Dirac cone. The origin of Dirac cone of our BNTs is different from those of CNTs.

The boron has three electrons in its outer most shell with the valence electron configuration $2s^2\ 2p^1$. Each boron atoms in this BNT structures has either six bonds or seven bonds. Simply, boron atoms can construct the sp^2 hybridize orbital by mixing the 2s, $2p_x$ and $2p_y$ orbitals. The $2p_z$ empty orbital does not contribute to the hybridization process. The sp^2 hybridizations of the boron atoms, are mainly contribute to the stability of the BNT structure forming hybrid bonds. Then hybridized sp^2 orbitals and empty p_z orbitals are interacting in an appropriate manner with electron cloud above or below the particular atom. This process may be the driven force to create the delocalized electron cloud. The electron exists in a cloud. The cloud spreads over the entire atom. The electron deficiency is forcing the electrons to be shared at the buckle surface. The apical atoms are acting as a bridge for the electron transfer within the two sub-lattices.

Delocalized electrons are often found in covalently bonded molecules. These covalent bonds are responsible for great stability of the borophene structure. Because of the delocalization, the electron density of BNT structure spreads over a great area by creating greater stability for the structure. There are no holes in this BNT structure otherwise buckling reduces the electron density. In addition, spreading electrons are creating the charge distribution. Delocalization of electrons also paves the way for the conductivity of the structure. Boron atoms are located on the straight line with coordination number six; they have the six neighboring atoms around them. The boron atoms in the zigzag line with coordination number seven and they have the seven neighboring atoms around them. It is impossible to appear the all bonds at the same time because the electron deficiency of the boron atom. The electron density between any neighboring atoms is higher than the over space.

The aromaticity of borophene structure is an important factor because it is not like the traditional aromaticity, which is caused by π orbitals in the prototypical aromatic molecules. The BNT structure has not only π aromatic, but also σ aromatic. Three sp^2 hybridized orbitals in each boron atom, are may be highly delocalized and look very similar to the π molecular orbital. As described in literature, the chemical bonding between the central atom and the pentagonal or hexagonal rings can be viewed as spokes of the molecule wheels. The double (π and σ) aromaticity is responsible for the novel buckled BNTs.

Various monolayer crystalline structures of boron with buckled and unbuckled surfaces, including the α-sheet, β-sheet, and γ-sheet, triangular sheet, or graphene–like

hexagonal sheet, have been predicted from *ab initio* computation. All of these boron sheets can be constructed by engraving different patterns of hexagonal holes within the triangular sheet and their hole densities can be described by a global density parameter, η. The parameter η is defined as the ratio of number of hexagons holes to the number of atomic sites in the pristine triangular sheet within unit cell of the decorated boron sheet. In addition, a local structural parameter, that is, the coordination number of boron atoms is used here to classify the BNTs into various types. For example, δ-type BNTs coordination numbers are four, five, and six along with β-type has a single value of coordination number. As a part of this research work, we constructed different BNTs from different boron sheets to compare the binding energies as tabulated in Table 5.2.

Table 5.2. The hole density (η) values, computed total energy (E_{total}), numbers of atoms in cell (N), and calculated binding energy ($E_{binding}$) for various BNTs.

BNTs	η	E_{total} (eV)	N	$E_{binding}$ (eV)
ω-BNT	0	-2457.8147	32	6.3146
δ_6-BNT	0	-1223.0160	16	5.9464
BNT (4,0)	0	-2457.4377	32	6.3028
δ_4-BNT	1/4	-1837.9655	24	6.0898
β-BNT	1/7	-4299.1522	56	6.2793
δ_3-BNT	1/2	-2432.5614	32	5.5254

The δ_3-BNT has the smallest cohesive energy of 5.5254 eV according to the Table 5.2 , indicating that the graphene-like structure is energetically unfavorable for BNTs. The ω-BNT has the largest cohesive energy among the six BNTs. The ω-BNT is a buckled tube with zero hole density. The BNT (4,0) has the second largest cohesive energy among them.

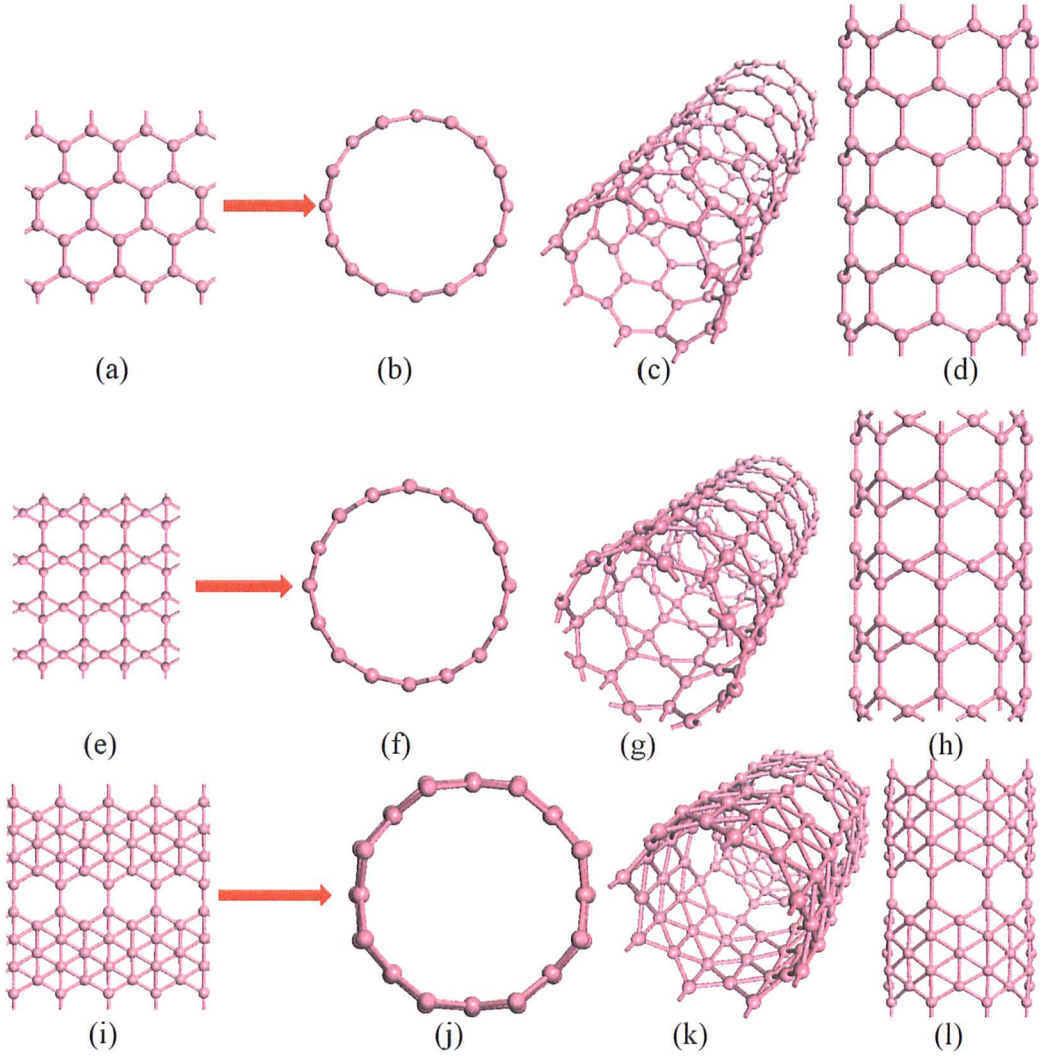

Figure 5.25. (a) δ_3-, (e) δ_4-, (i) β- type boron monolayer sheets. (b) δ_3-, (f) δ_4-, (j) β-BNTs of top view of cross section. (c,d) δ_3-, (g,h) δ_4-, (k,l) β- BNTs of side view.

It is important to mention that we were able to find another lower energy BNT by starting from the δ_6-boron sheet as shown in Figure 5.26. Original δ_6-boron sheet is buckled monolayer structure. In this case, we did some modification for the δ_6-boron sheet. As a first step, we converted δ_6-boron sheet in to unbuckled monolayer plane sheet. Afterwards, moved red color atoms (see Figure 5.26) inward from the plane, resulting in another buckled boron sheet. The novel boron sheet is designated as ω-sheet. The coordination numbers of boron atoms are six and eight in the ω-sheet. Finally, we rolled up this buckled ω-sheet and reconnected the boron atoms as depicted in Figure 5.26. The constructed tube is named as ω-BNT.

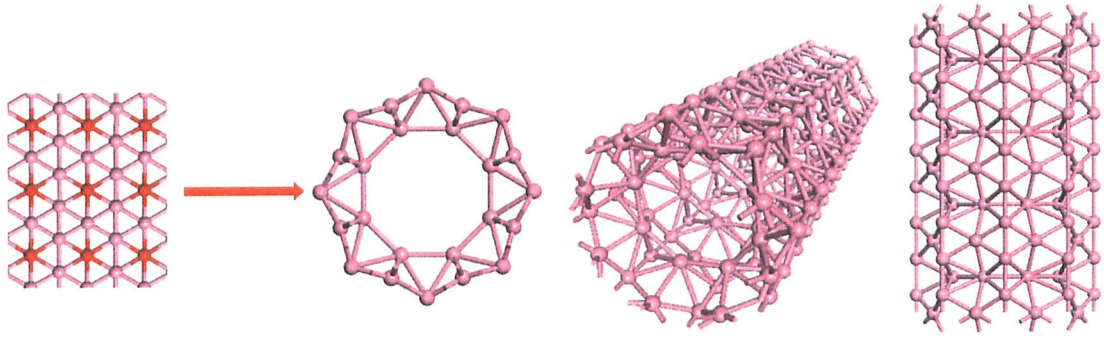

Figure 5.26. (a) Boron monolayer sheet. Red color denotes boron atoms moving inward from the plane, (b) Top view of the cross section of ω-BNT, (c) Perspective, and (d) side views of the ω-BNT.

The calculated electronic band structure of the ω-BNT is shown Figure 5.27. The Dirac cone lies slightly below the Fermi level that means particular structure is self-doped and electrons are present as charge carriers.

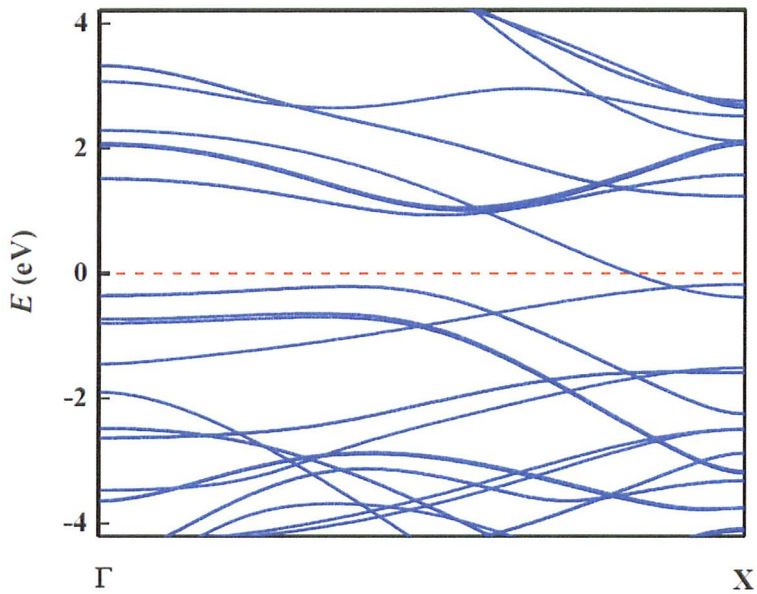

Figure 5.27. (Color line) Calculated band structures of ω-BNT. Γ= (0, 0), X= (0, π/a), where a = 3.24 Å. The Fermi level is shifted to 0 eV (dashed red line).

5.4 Conclusion

We have performed a first principle based global research of lowest energy structures of the BNTs. Within the scope of our research, all the nanotubes derived from borophene sheet are metallic or semimetallic. Our theoretical calculations show that the BNTs derived from borophene have a Dirac cone at the Fermi level. The quasi particle group velocity is comparable to that in graphene, but strongly direction dependent. The buckling and coupling between the two constituent sublattices are the key factors for the energetic stability and the emergence of the Dirac cone.

CHAPTER 6

SUMMARY AND FUTURE WORK

In this thesis, we focused our investigations on two systems. One is the magnetic and electronic properties of nitrophenyl functionalized graphene, and the other is boron nanotubes.

Nitrophenyl functionalization of epitaxial graphene not only provides a route for band gap engineering, but also leads to magnetism in the graphene sheet including antiferromagnetic and ferromagnetic regions. The optimization of the chemical functionalization of the epitaxial wafers may induce long-range ferromagnetic order combined with periodic semiconductors, thereby leading to advanced spintronic devices. Our theoretical investigations have clarified structures with ferromagnetism and antiferromagnetism in graphene. The covalent functionalization leads to unpaired spins, which is useful to engineering electronic and magnetic devices such as ferromagnetic semiconductors in an organic macromolecule.

The investigation of nitrophenyl functionalization of graphene provides a proof of concept for the graphene-based spintronics. The fundamental concept is to redirect the electronic conjugation pathway and to form specific conducting, insulating, and magnetic patterns. To tune the band gap, future advances in the experimental research will require a more detailed understanding of the electronic and magnetic properties of nitrophenyl functionalization of graphene.

We have investigated novel BNTs structures derived from boron quasi planner structure. Investigations of various chemical species differing from those discussed in this thesis will be useful. Boron nanostructures can be used in applications such as specialized electrodes in batteries or as lithium storage. There may be novel boron materials in the form of boron sheets and boron nanotubes, which are still waiting to be experimentally observed or synthesized.

REFERENCES

1. Neto, A. H. C.; Guinea, F.; Peres, N. M. R.; Novoselov, K. S.; Geim, A. K. The Electronic Properties of Graphene. *Rev. Mod. Phys.* **2009**, *81*, 109.
2. Geim, A. K.; Novoselov, K. S. The Rise of Graphene. *Nat. Mater.* **2007**, *6*, 183-191.
3. Rao, C. N. R.; Sood, A. K.; Subrahmanyam, K. S.; Govindaraj, A. Graphene: The New Two-Dimensional Nanomaterial. *Angew. Chem., Int. Ed.* **2009**, *48*, 7752.
4. Allen, M. J.; Tung, V. C.; Kaner, R. B. Honeycomb Carbon: a Review of Graphene. *Chem. Rev.* **2010**, *110*, 132.
5. Oostinga, J. B.; Heersche, H. B.; Liu, X.; Morpurgo, A. F.; Vandersypen, L. M. Gate-Induced Insulating State in Bilayer Graphene Devices. *Nat. Mater.* **2008**, *7*, 151.
6. Berger, C.; Song, Z.; Li, X.; Wu, X.; Brown, N., Naud, C.; Mayou, D.; Li, T.; Hass, J.; Marchenkov, A. N.; Conrad, E. H; First, P. N.; de Heer, W. A. Electronic Confinement and Coherence in Patterned Epitaxial Graphene. *Science* **2006**, *312*, 1191.
7. Leenaerts, O.; Partoens, B.; Peeters, F. M. Hydrogenation of Bilayer Graphene and the Formation of Bilayer Graphane from First Principles. *Phys. Rev. B* **2009**, *80*, 24.

8. Li, X.; Wang, X.; Zhang, L.; Lee, S.; Dai, H. Chemically Derived, Ultrasmooth Graphene Nanoribbon Semiconductors. *Science* **2008**, *319*, 1229.

9. Xia, F.; Farmer, D. B.; Lin, Y.-M.; Avouris, P. Graphene Field-Effect Transistors with High On/Off Current Ratio and Large Transport Band Gap at Room Temperature, *Nano Lett.* **2010**, *10*, 715.

10. Wang, X.; Ouyang, Y.; Li, X.; Wang, H.; Guo, J.; Dai, H. Room-Temperature All-Semiconducting Sub-10 nm Graphene Nanoribbon Field-Effect Transistors. *Phys. Rev. Lett.* **2008**, *100*, 206803.

11. Castro, E. V.; Novoselov, K. S.; Morozov, S. V.; Peres, N. M. R.; dos Santos, J. M. B. L.; Nilsson, J.; Guinea, F.; Geim, A. K.; Neto, A. H. C. Biased Bilayer Graphene: Semiconductor with a Gap Tunable by the Electric Field Effect. *Phys. Rev. Lett.* **2007**, *99*, 216802.

12. Zhang, Y.; Tang, T.-T.; Girit, C.; Hao, Z.; Martin, M. C.; Zettl, A.; Crommie, M. F.; Shen, Y. R.; Wang, F. Direct Observation of a Widely Tunable Bandgap in Bilayer Graphene. *Nature* **2009**, *459*, 820.

13. Mak, K. F.; Lui, C. H.; Shan, J.; Heinz, T. F. Observation of an Electric-Field-Induced Band Gap in Bilayer Graphene by Infrared Spectroscopy. *Phys. Rev. Lett.* **2009**,*102*, 256405.

14. Samarakoon, D. K.; Wang, X.-Q. Tunable Band Gap in Hydrogenated Bilayer Graphene. *ACS Nano* **2010**, *4*, 4126.

15. Elias, D. C.; Nair, R. R.; Mohiuddin, T. M. G.; Morozov, S. V.; Blake, P.; Halsall, M. P.; Ferrari, A. C.; Boukhvalov, D. W.; Katsnelson, M. I.; Geim, A. K.;

16. Novoselov, K. S. Control of Graphenes Properties by Reversible Hydrogenation: Evidence for Graphane. *Science* **2009**, *323*, 610.

17. Liu, L.-H.; Yan, M.-D. A Simple Method for the Covalent Immobilization of Graphene. *Nano Lett.* **2009**, *9*, 3375.

18. Bekyarova, E.; Sarkar, S.; Niyogi, S.; Itkis, M. E.; Haddon, R.C. Advances in the Chemical Modification of the Epitaxial Graphene. *J. Phys. D: Appl. Phys.* **2012**, *45*, 154009.

19. Hong, J.; Niyogi, S.; Itkis, M. E.; Bekyarova, E.; Ramesh, P.; Amos, N.; Litvinov, D.; Berger C.; de Heer, W. A.; Haddon, R.C.; Khizroev, S. Effect of Nitrophenyl Functionalization on the Magnetic Properties of Epitaxial Graphene. *Small* **2011**,*7*,1175

20. Niyogi, S.; Bekyarova, E.; Hong, J.; Khizroev, S.; Berger, C.; de Heer, W. A. Covalent Chemistry for Graphene Electronics. *J. Phys. Chem. Lett.* **2011**, *2*, 2487.

21. Dugaev, V.K.; Litvinov, V.I.; Barnas, J. Exchange Interaction of Magnetic Impurities in Graphene. *Phys. Rev. B* **2006**, *74*, 224438.

22. Yazyev, O.V.; Helm L. Defect-induced Magnetism in Graphene. *Phys. Rev. B* **2007**, *75*, 125408.

23. Vozmediano, M.A.H.; L-Sancho, M.P.; Stauber, T.; Guinea, F. Local Defects and Ferromagnetism in Graphene Layers. *Phys. Rev. B* **2007**, *72*, 155121.

24. Singh, R.; Kroll, P. Magnetism in Graphene due to Single Atom Defects: Dependance on the Concentration and Packing Geometry of Defects. *J. Phys.: Condens. Matter* **2009**, *21*, 196002.

25. Hong, J.; Bekyarova, E.; de Heer, W. A.; Haddon, R.C.; Khizroev, S. Chemically Engineered Graphene-Based 2D Organic Molecular Magnet. *ACS Nano* **2013**, *7*, 10011.

26. Li, L.; Qin, R.; Li, H.; Yu, L.; Liu, Q.; Luo, G.; Gao, Z.; Lu, J. Functionalized Graphene for High-performance Two-Dimensional Spintronics Devices. *ACS Nano* **2011**, *5*, 2610.

27. Morita, Y.; Suzuki, S.; Sato, K.; Takui, T. Synthetic Organic Spin Chemistry for Structurally well-defined open-shell Graphene Fragments. *Nature Chem.* **2011**, *3*, 197.

28. He, H.; Gao, C. General Approach to Individually Dispersed, Highly Soluble, and Conductive Graphene Nanosheets Functionalized by Nitrene Chemistry. *Chem. Mater.* **2010**, *22*, 5054.

29. Quintana, M.; Spyrou, K.; Marek Grzelczak, M.; Browne, W. R.; Rudolf, P.; Prato, M. Functionalization of Graphene *via* 1,3-Dipolar Cycloaddition. *ACS Nano* **2010**, *4*, 3527.

30. Choi, J.; Kim, K.-J.; Kim, B.; Lee, H.; Kim, S. Covalent Functionalization of Epitaxial Graphene by Azidotrimethylsilane. *J. Phys. Chem. C* **2009**, *113*, 9433.

31. Liu, L.-H.; Lerner, M. M.; Yan, M. Derivitization of Pristine Graphene with Well-Defined Chemical Functionalities. *Nano Lett.* **2010**, *10*, 3754.

32. Partoens, B.; Peeters, F. M. From Graphene to Graphite: Electronic Structure around the K Point. *Phys. Rev. B* **2006**, *74*, 075404.

33. Flores, M. Z. S.; Autreto, P. A. S.; Legoas, S. B.; Galvao, D. S. Graphene to Graphane: a Theoretical Study. *Nanotechnology* **2009**, *20*, 465704.

34. Samarakoon, D. K.; Wang, X.-Q. Chair and Twisted-Boat Membranes in Hydrogenated Graphene. *ACS Nano* **2009**, *3*, 4017.

35. Lee, Y.-S.; Marzari, N. Cycloaddition Functionalizations to Preserve or Control the Conductance of Carbon Nanotubes. *Phys. Rev. Lett.* **2006**, *97*, 116801.

36. Park, H.; Zhao, J.; Lu, J.-P. Effects of Sidewall Functionalization on Conducting Properties of Single Wall Carbon Nanotubes. *Nano Lett.* **2006**, *6*, 916.

37. Ogunro, O. O.; Wang, X.-Q. Quantum Electronic Stability in Selective Enrichment of Carbon Nanotubes. *Nano Lett.* **2009**, *9*, 1034.

38. Ogunro, O. O.; Karunwi, K.; Khan, I. M.; Wang, X.-Q. Chiral Asymmetry of Helical Polymer Nanowires. *J. Phys. Chem. Lett.* **2010**, *1*, 704.

39. Suggs, K.; Wang, X.-Q. Structural and Electronic Properties of Carbon Nanotube-Reinforced Epoxy Resins. *Nanoscale* **2010**, *2*, 385.

40. DMol3, Accelrys Software Inc., San Diego, CA, **2010**.

41. Perdew, J. P.; Burke, K.; Ernzerhof, M. Generalized Gradient Approximation Made Simple. *Phys. Rev. Lett.* **1996**, *77*, 3865.

42. Saremi, S. RKKY in half-filled bipartite lattices: Graphene as an example. *Phys. Rev. B* **2007**, *76*, 184430.

43. Boustani, I. A comparative study of *Ab initio* SCF-CI and DFT. Example of Small Boron Clusters. *Chem. Phys. Lett.* **1995**, *233*, 273.

44. Boustani, I. Structure and Stability Of Small Boron Clusters. A Density Functional Theoretical Study. *Chem. Phys. Lett.* **1995**, *240*, 135.

45. Boustani, I. New Quasi-Planar Surfaces of Bare Boron. *Surf. Sci.* **1997**, *370*, 355.

46. Boustani, I. Systematic *Ab initio* Investigation of Bare Boron Clusters: Determination of The Geometry and Electronic Structures of B_n $(n = 2\text{-}14)$, *Phys. Rev. B* **1997**, *55*, 16426.

47. Zhou, X.; Dong, X.; Oganov, A. R.; Zhu, Q.; Tian, Y.; Wang, H. Semimetallic Two – Dimensional Boron Allotrope with Massless Dirac Fermions. *Phys. Rev. Lett.* **2014**, *112*, 085502.

48. Zhai, H. J.; Wang, L. S.; Alexandrova, A. N.; Boldyrev, A. I. Electronic Structure and Chemical Bonding of B_5^- and B_5 by Photoelectron Spectroscopy and *Ab initio* Calculations. *J. Chem. Phys.* **2002**, *117*, 7917.

49. Zhai, H. J.; Kiran, B.; Li, J. L.; Wang, L. S. Hydrocarbon Analogues of Boron Clusters-Planarity, Aromaticity and Antiaromaticity. *Nature Mater.* **2003**, *2*, 827.

50. Zhai, H.-J.; Alexandrova, A. N.; Birch, K. A.; Boldyrev, A. I.; Wang, L.S. Hepta- and Octacoordinate Boron in Molecular Wheels of Eight- and Nine-Atom Boron Clusters: Observation and Confirmation. *Angew.Chem. Int. Ed.* **2003**, *42*, 6004.

51. Alexandrova, A. N.; Boldyrev, A. I.; Zhai, H. J.; Wang, L. S. Electronic Structure, Isomerism, and Chemical Bonding in B_7^-- and B_7. *J. Phys. Chem. A* **2004**, *108*, 3509.

52. Penev, E. S.; Bhowmick, S.; Sadrazadeh, A.; Yakobson, B. I. Polymophism of Two – Dimensional Boron. *Nano. Lett.* **2012**, *12*, 2441.

53. Kiran, B.; Bulusu, S.; Zhai, H. J.; Yoo, S.; Zeng, X. C.; Wang, L. S. Planar-to-tubular Structural Transition in Boron Clusters: B_{20} as The Embryo of Single-Walled Boron Nanotubes. *Proc. Natl. Acad. Sci. U.S.A.* **2005**, *102*, 961.

54. Aihara, J.-I.; Kanno, H.; Ishida, T. Aromaticity of Planar Boron Clusters Confirmed. *J. Am. Chem. Soc.* **2005**, *127*, 13324.

55. Boustani, I.; Quandt, A.; Rubio, A. Boron Quasicrystals and Boron Nanotubes: *Ab initio* Study of Various B_{96} Isomers. *J. Solid State Chem.* **2000**, *154*, 269.

56. Chacko, S.; Kanhere, D. G.; Boustani, I. *Ab initio* Density Functional Investigation of B_{24} Clusters: Rings, Tubes, Planes, and Cages. *Phys. Rev. B* **2003**, *68*, 035414.

57. Tian F.-Y.; Wang, Y.-X. The Competition of Double-, Four-, and Three-ring Tubular B_{3n} (n=8–32) Nanoclusters. *J. Chem. Phys.* **2008**, *129*, 024903.

58. Boustani I.; Quandt, A. Nanotubules of Bare Boron Clusters: *Ab initio* and Density Functional Study. *Europhys. Lett.* **1997**, *39*, 527.

59. Gindulytė, A.; Lipscomb, W. N.; Massa, L. Proposed Boron Nanotubes. *Inorg. Chem.* **1998**, *37*, 6544.

60. Boustani, I.; Quandt, A.; Hernandez, E.; Rubio, A. New Boron Based Nanostructured Materials. *J. Chem. Phys.* **1999**, *110*, 3176.

61. Boustani I.; Quandt, A. Boron in *Ab initio* Calculations. *Comput. Mater. Sci.* **1998**, *11*, 132.

62. Quandt A.; Boustani, I. Boron Nanotubes. *Chem. Phys. Chem.* **2005**, *6*, 2001.

63. Ciuparu, D.; Klie, R. F.; Zhu, Y.; Pfefferle, L. Synthesis of Pure Boron Single-Wall Nanotubes. *J. Phys. Chem. B* **2004**, *108*, 3967.

64. Evans, M. H.; Joannopoulos, J. D.; Pantelides, S. T. Electronic and Mechanical Properties of Planar and Tubular Boron Structures. *Phys. Rev. B* **2005**, *72*, 045434.

65. Kunstmann J.; Quandt, A. Constricted Boron Nanotubes. *Chem. Phys. Lett.* **2005**, *402*, 21.

66. Kunstmann J.; Quandt, A. Broad Boron Sheets and Boron Nanotubes: An *ab initio* Study of Structural, Electronic, and Mechanical Properties. *Phys. Rev. B* **2006**, *74*, 035413.

67. Lau K. C.; Pandey, R. Stability and Electronic Properties of Atomistically-Engineered 2D Boron Sheets. *J. Phys. Chem. C* **2007**, *111*, 2906.

68. Cabria, I.; Lopez, M. J.; Alonso, J. A. Density Functional Calculations of Hydrogen Adsorption on Boron Nanotubes and Boron Sheets. *Nanotechnology* **2006**, *17*, 778.

69. Sebetci, A.; Mete, E.; Boustani, I. Free Standing Double Walled Boron Nanotubes. *J. Phys. Chem. Solids* **2008**, *69*, 2004.

70. Gonzalez Szwacki, N.; Sadrzadeh, A.; Yakobson, B. I. B_{80} Fullerene: An *Ab initio* Prediction of Geometry, Stability, and Electronic Structure. *Phys. Rev. Lett.* **2007**, *98*, 166804.

71. Tang H.; Ismail-Beigi, S. Novel Precursors for Boron Nanotubes: The Competition of Two-Center and Three-Center Bonding in Boron Sheets. *Phys. Rev. Lett.* **2007**, *99*, 115501.

72. Yang, X.; Ding, Y.; Ni, J. *Ab initio* Prediction of Stable Boron Sheets and Boron Nanotubes: Structure, Stability, and Electronic Properties. *Phys. Rev. B* **2008**, *77*, 041402(R).

73. Yan, Q.-B.; Sheng, X.-L.; Zheng, Q.-R.; Zhang, L.-Z.; Su, G. Family of Boron Fullerenes: General Constructing Schemes, Electron Counting Rule, and *Ab initio* Calculations. *Phys. Rev. B* **2008**, *78*, 201401(R).

74. Zope, R. R. The α-boron Cages with Four-member Rings. *EPL* **2009**, *85*, 68005.

75. Zope, R. R.; Baruah, T.; Lau, K. C.; Liu, A. Y.; Pederson, M. R.; Dunlap, B. I. Boron fullerenes: From B_{80} to Hole Doped Boron Sheets. *Phys. Rev. B* **2009**, *79*, 161403(R).

76. Tang H.; Ismail-Beigi, S. Self-doping in Boron Sheets from First Principles: A Route to Structural Design of Metal Boride Nanostructures. *Phys. Rev. B* **2009**, *80*, 134113.

77. Singh, A. K.; Sadrzadeh, A.; Yakobson, B. I. Probing Properties of Boron α-Tubes by *Ab initio* Calculations. *Nano Lett.* **2008**, *8*, 1314.

78. Li, M.; Li, Y.; Zhou, Z.; Shen, P.; Chen, Z. Ca-Coated Boron Fullerenes and Nanotubes as Superior Hydrogen Storage Materials. *Nano Lett.* **2009**, *9*, 1944.

79. Li, Y.; Zhou, G.; Li, J.; Gu, B.-L.; Duan, W. Alkali-Metal-Doped B_{80} as High-Capacity Hydrogen Storage Media. *J. Phys. Chem. C* **2008**, *112*, 19268.

80. Geim, K.; Novoselov, K. S. The Rise of Graphene. *Nat. Mater.* **2007**, *6*, 183.

81. Novoselov, K. S.; Geim, A.; Morozov, S.; Jiang, D.; Katsnelson, M.; Grigorieva, I.; Dubonos, S.; Firsov, A. Two-Dimensional Gas of Massless Dirac Fermions in Graphene. *Nature* **2005**, *438*, 197.

82. Berger, C; Song, Z.; Li, X.; Wu, X.; Brown, N.; Naud, C.; Mayou, D.; Li, T.; Hass, J.; Marchenkov, A. N.; Conrad, E. H.; First, P. N.; de Heer, W. A. Electronic Confinement and Coherence in Patterned Epitaxial Graphene. *Science* **2006**, *312*, 1191.

83. Schedin, F.; Geim, A. K.; Morozov, S. V.; Hill, E. W.; Blake, P.; Katsnelson M. I.; Novoselov, K. S. Detection of Individual Gas Molecules Adsorbed on Graphene. *Nat. Mater.* **2007**, *6*, 652.

84. Schwierz, F. Graphene Transistors. *Nat. Nanotechnol.* **2010**, *5*, 487.

85. Balandin, A. A.; Ghosh, S.; Bao, W.; Calizo, I.; Teweldebrhan, D.; Miao F.; Lau, C. N. Dimensional Crossover of Thermal Transport in Few-Layer Graphene Materials. *Nano Lett.* **2008**, *8*, 902.

86. Recher, P.; Trauzettel B.; Blaner Y. M.; Beenakker C. W. J.; Morpurgo A. F. Aharonov-Bohm effect and broken valley degeneracy in graphene rings *Phys. Rev. B* **2007,** *76*, 235404.

87. Pereira, M. J.; Vasilopoulos, P; Peeters F.M. Tunable Quantum Dots in Bilayer Graphene. *Nano Lett.* **2007**, *7*, 946.

88. Shao, Q.; Liu, G.; Teweldebrhan D.; Balandin, A. A. High-Temperature Quenching of Electrical Resistance in Graphene Interconnects. *Appl. Phys. Lett.* **2008**, *92*, 202108.

89. Wang, X.; Zhi L.; Mullen, K. Transparent, Conductive Graphene Electrodes for Dye-Sensitized Solar Cells. *Nano Lett.* **2008**, *8*, 323.

90. Allinger, N. L. *Molecular Structure: Understanding Steric and Electronic Effects from Molecular Mechanics*; John Wiley & Sons: Hoboken, **2010**.

91. Bauschlicher Jr., C. W. and Langhoff, S. R. Quantum Mechanical Calculations to Chemical Accuracy. *Science* **1991**, *254*, 394.

92. Cramer, C. J. *Essentials of Computational Chemistry: Second Edition Theory and Models*; John Wiley & Sons, Ltd.: West Sussex, 2004; pp 596

93. Bachrach, S. M. *Computational Organic Chemistry*; John Wiley & Sons, Inc.: Hoboken, **2007**; pp 478

94. Perdew, J. P.; Burke, K.; Ernzerhof, M. Generalized Gradient Approximation Made Simple. *Phys. Rev. Lett.* **1996**, *77*, 3865.

95. Gunasinghe, R. N.; Reuven, D. G.; Suggs, K.; Wang, X.-Q. Filled and Empty Orbital Interactions in a Planar Covalent Organic Framework on Graphene. *J. Phys. Chem. Lett.* **2012**, *3*, 3048.

96. Hargrove, J.; Shashikala, H. B. M.; Guerrido, L.; Ravi, N.; Wang, X.-Q. Tunable Doping in Graphene by Light-Switchable Molecules. *Nanoscale* **2012**, *4*, 4443–4446.

97. Kohn, W. Nobel Lecture: Electronic Structure of Matter – wave Functions and Density Functionals. *Rev. Mod. Phys.* **1999**, *71*, 1253-1266.

98. Perdew, J. and Zunger, A. Self-interaction Correction to Density Functional Approximations for Many-electron Systems. *Phys. Rev. B* **1981**, *23*, 5048-5079.

99. Vosko, S.; Wilk, L. and Nusair M. Accurate Spin-dependent Electron Liquid Correlation Energies for Local Spin Density Calculations: A Critical Analysis. *Can. J. Phys.* **1980**, *58*, 1200-1211.

100. Krasheninnikov A. *Computational Methods for Material Sciences*; University of Helsinki: Helsinki, 2000.

101. Nathaniel, J. and Wang, X.-Q. Tunable Electron and Hole Doping in $FeCl_3$ Intercalated Graphene. *Appl. Phys. Lett.* **2012**, *100*, 213112-213113.

102. Hiranandani, D.; Salimath, A.; Bishnoi, B.; Nandal, V.; Akram, M. W.; Jayanthi, A.; Yada, M. K. and Ghosh, B. Magnonscattering in Single and Bilayer Graphene Intercalates. *J. Appl. Phys.* **2012**, *112*, 114308–114309.

103. Huang, Q. S.; Chen, X. L.; Lin, J. J.; Li, K.; Jia, Y.P.; Liu, J.; Guo, L.W.; Wang, W.J. and Wang, G. Preparation of Quasi-Free-Standing Graphene with a Super Large Interlayer Distance by Methane Intercalation. *J. Phys. Chem. C* **2011**, *115*, 20538-20545.

104. Kroto, H. W.; Heath, J. R.; O'Brien, S. C.; Curl, R. F.; Smalley, R. E. C_{60}: Buckminsterfullerene. *Nature* **1985**, *318*, 162-163.

105. Iijima, S. Helical Microtubules of Graphitic Carbon. *Nature* **1991**, *354*, 56-58.

106. Novoselov, K. S.; Geim, A. K.; Morozov, S. V.; Jiang, D.; Katsnelson, M. I.; Grigorieva, I. V.; Dubonos, S. V.; Firsov, A. A. Two-Dimensional Gas of Massless Dirac Fermions in Graphene. *Nature* **2005**, *438*, 197-200.

107. Röthlisberger, U.; Andreoni, W.; Parrinello, M. Structure of Nanoscale Silicon Clusters. *Phys. Rev. Lett.* **1994**, *72*, 665-668.

108. Yoo, S.; Zhao, J. J.; Wang, J. L.; Zeng, X. C. Endohedral Silicon Fullerenes SiN ($27 < N < 39$). *J. Am. Chem. Soc.* **2004**, *126*, 13845-13849.

109. Jackson, K. A.; Horoi, M.; Chaudhuri, I.; Frauenheim, T.; Shvartsburg, A. A. Unraveling the Shape Transformation in Silicon Clusters. *Phys. Rev. Lett.* **2004**, *93*, 013401.

110. Sun, Q.; Wang, Q.; Jena, P.; Rao, B. K.; Kawazoe, Y. Stabilization of Si_{60} Cage Structure. *Phys. Rev. Lett.* **2003**, *90*, 135503.

111. Saranin, A. A.; Zotov, A. V.; Kotlyar, V. G.; Kasyanova, T. V.; Utas, O. A.; Okado, H.; Katayama, M.; Oura, K. Ordered Arrays of Be-Encapsulated Si Nanotubes on Si(111) Surface. *Nano Lett.* **2004**, *4*, 1469-1473.

112. Bai, J.; Zeng, X. C.; Tanaka, H.; Zeng, J. Y. Metallic Single-Walled Silicon Nanotubes. *Proc. Natl. Acad. Sci. U.S.A.* **2004**, *101*, 2664-2668.

113. Bai, J.; Tanaka, H.; Zeng, X. C. Graphene-like Bilayer Hexagonal Silicon Polymorph. *Nano Res.* **2010**, *3*, 694-700.

114. Boustani, I. New Quasi-Planer Surfaces of Bare Boron. *Surf. Sci.* **1997**, *370*, 355-363.

115. Boustani, I. Towards Novel Boron Nanostructural Materials. *Chem. Modell.* **2011**, *8*, 1-44.

116. Zhai, H. J.; Kiran, B.; Li, J.; Wang, L. S. Hydrocarbon Analogues of Boron Clusters-Planarity, Aromaticity and Antiaromaticity. *Nat. Mater.* **2003**, *2*, 827-833.

117. Zhai, H. J.; Alexandrova, A. N.; Birch, K. A.; Boldyrev, A. I.; Wang, L. S. Hepta- and Octacoordiante Boron in Molecular Wheels of Eight- and Nine Boron Clusters: Observation and Confirmation. *Angew. Chem., Int. Ed.* **2003**, *42*, 6004-6008.

118. Huang, W.; Sergeeva, A. P.; Zhai, H. J.; Averkiev, B. B.; Wang, L. S.; Boldyrev, A. I. A Concentric Planer Doubly π Aromatic B_{19} Cluster. *Nat. Chem.* **2010**, *2*, 202-206.

119. Alexandrova, A. N.; Boldyrev, A. I.; Zhai, H. J.; Wang, L. S. All-Boron Aromatic Clusters as Potential New Inorganic Ligands and Building Blocks in Chemistry. *Coord. Chem. Rev.* **2006**, *250*, 2811-2866.

120. Galeev, T. R.; Chen, Q.; Guo, J. G.; Bai, H.; Miao, C. Q.; Lu, H. G.; Sergeeva, A. P.; Li, S. D.; Boldyrev, A. I. Deciphering the Mystery of Hexagon Holes in an All-Boron Graphene R-Sheet. *Phys. Chem. Chem. Phys.* **2011**, *13*, 11575-11578.

121. Szwacki, N. G.; Sadrzadeh, A.; Yakobson, B. I. B_{80} Fullerene: An *Ab Initio* Prediction of Geometry, Stability, and Electronic Structure. *Phys. Rev. Lett.* **2007**, *98*, 166804.

122. Szwacki, N. G. Boron Fullerenes: A First-Principles Study. *Nanoscale Res. Lett.* **2008**, *3*, 49-54.

123. Yan, Q. B.; Sheng, X. L.; Zheng, Q. R.; Zhang, L. Z.; Su, G. Family of Boron Fullerenes: General Constructing Schemes, Electron Counting Rule, and Ab Initio Calculations. *Phys. Rev. B* **2008**, *78*, 201401(R).

124. Sadrzadeh, A.; Pupysheva, O. V.; Singh, A. K.; Yakobson, B. I. The Boron Buckyball and Its Precursors: An Electronic Structure Study. *J. Phys. Chem. A* **2008**, *112*, 13679-13683.

125. Jin, P.; Hao, C.; Gao, Z. X.; Zhang, S. B.; Chen, Z. F. Endohedral Metalloborofullerenes La2@B_{80} and Sc3N@B_{80}: A Density Functional Theory Prediction. *J. Phys. Chem. A* **2009**, *113*, 11613-11618.

126. Li, H.; Shao, N.; Shang, B.; Yuan, L. F.; Yang, J. L.; Zeng, X. C. Icosahedral B_{12}-Containing CoreShell Structures of B_{80}. *Chem. Commun.* **2010**, *46*, 3878-3880.

127. Zhao, J. J.; Wang, L.; Li, F. Y.; Chen, Z. F. B_{80} and Other Medium-Sized Boron Clusters: CoreShell Structures, Not Hollow Cage. *J. Phys. Chem. A* **2010**, *114*, 9969-9972.

128. Boustani, I. Systematic Ab Initio Investigation of Bare Boron Clusters: Determination of the Geometry and Electronic Structures of B_n (n=2-14). *Phys. Rev. B* **1997**, *55*, 16426-16438.

129. Boustani, I.; Quandt, A. Nanotubules of Bare Boron Clusters: *Ab Initio* and Density Functional Study. *Europhys. Lett.* **1997**, *39*, 527-532.

130. Kiran, B.; Bulusu, S.; Zhai, H. J.; Yoo, S.; Zeng, X. C.; Wang, L. S. Planar-to-Tubular Structural Transition in Boron Clusters: B_{20} as the Embryo of Single-Walled Boron Nanotubes. *Proc. Natl. Acad. Sci. U.S.A.* **2005**, *4*, 961-964.

131. Oger, E.; Crawford, N. R. M.; Kelting, P.; Weis, P.; Kappes, M. M.; Ahlrichs, R. Boron Cluster Cations: Transition from Planer to Cylindrical Structures. *Angew. Chem., Int. Ed.* **2007**, *46*, 8503-8506.

132. An, W.; Bulusu, S.; Gao, Y.; Zeng, X. C. Relative Stability of Planar versus Double-Ring Tubular Isomers of Neutral and Anionic Boron Cluster B_{20} and B_{20}^-. *J. Chem. Phys.* **2006**, *124*, 154310.

133. Piazza, Z. A.; Hu, H. S.; Li, W. L.; Zhao, Y. F.; Li, J.; Wang, L. S. Planar Hexagonal B_{36} as a Potential Basis for Extended Single-atom Layer Boron Sheets. *Nat. Commun.* **2014**, *5*, 3113.

134. Wang, Y. C.; Lv, J.; Zhu, L.; Ma, Y. M. Crystal Structure Prediction via Particle-Swarm Optimization. *Phys. Rev. B* **2010**, *82*, 094116.

135. Luo, X.; Yang, J.; Liu, H.; Wu, X. J.; Wang, Y. C.; Ma, Y. M.; Wei, S. H.; Gong, X. G.; Xiang, H. J. Predicting Two-Dimensional BoronCarbon Compounds by Global Optimization Method. *J. Am. Chem. Soc.* **2011**, *133*, 16285–16290.

136. Oganov, A. R.; Chen, J.; Gatti, C.; Ma, Y. Z.; Ma, Y. M.; Glass, C. W.; Liu, Z.; Yu, T.; Kurakevych, O. O.; Solozhenko, V. L. Ionic High-Pressure Form of Elemental Boron. *Nature* **2009**, *457*, 863–867.

137. Wang, Y. C.; Liu, H. Y.; Lv, J.; Wang, H.; Ma, Y. M. High Pressure Partially Ionic Phase of Water Ice. *Nat. Commun.* **2011**, *2*, 563.

138. Zhu, L.; Wang, Z.; Wang, Y. C.; Zou, G. T.; Mao, H.; Ma, Y. M. Spiral Chain O4 Form of Dense Oxygen. *Proc. Natl. Acad. Sci. U.S.A.* **2012**, *3*, 751–753.

139. Kresse, G.; Furthmüller, J. Efficiency of Ab Initio Total Energy Calculations for Metals and Semiconductors Using a Plane-Wave Basis Set. *J. Comput. Mater. Sci.* **1996**, *6*, 15–50.

140. Kresse, G.; Furthmüller, J. Efficient Iterative Schemes for Ab initio Total-Energy Calculations Using a Plane-Wave Basis Set. *Phys. Rev. B* **1996**, *54*, 11169-11186.

141. Hohenberg, P.; Kohn, W. Inhomogeneous Electron Gas. *Phys. Rev.* **1964**, *136*, B864-B871.

142. Kohn, W.; Sham, L. J. Self-Consistent Equations Including Exchange and Correlation Effects. *Phys. Rev.* **1965**, *140*, A1133-A1138.

143. Payne, M. C.; Teter, M. P.; Allan, D. C.; Arias, T. A.; Joannopoulos, J. D. Iterative Minimization Techniques for Ab Initio Total-Energy Calculations: Molecular Dynamics and Conjugate Gradients. *Rev. Mod. Phys.* **1992**, *64*, 1045-1097.

144. Clark, S. J.; Segall, M. D.; Pickard, C. J.; Hasnip, P. J.; Probert, M. J.; Refson, K.; Payne, M. C. First Principles Methods Using CASTEP. *Z. Kristallogr.* **2005**, *220*, 567-570.

145. Pfrommer, B. G.; Cote, M.; Louie, S. G.; Cohen, M. L. Relaxation of Crystals with the Quasi-Newton Method. *J. Comput. Phys.* **1997**, *131*, 233-240.

146. Vanderbilt, D. Soft Self-Consistent Pseudopotentials in a Generalized Eigenvalue Formalism. *Phys. Rev. B* **1990**, *41*, 7892-7895.

147. Perdew, J. P.; Burke, K.; Ernzerhof, M. Generalized Gradient Approximation Made Simple. *Phys. Rev. Lett.* **1996**, *77*, 3865-3868.

148. Monkhorst, H. J.; Pack, J. D. Special Points for Brillouin-Zone Integrations. *Phys. Rev. B* **1976**, *13*, 5188-5192.

149. Adamo, C.; Barone, V. Toward Reliable Density Functional Methods without Adjustable Parameters: The PBE0 Model. *J. Chem. Phys.* **1999**, *110*, 6158-6170.

150. Troullier, N.; Martins, J. L. Efficient Pseudopotentials for Plane-Wave Calculations. *Phys. Rev. B* **1991**, *43*, 1993-2006.

151. Tkatchenko, A.; Scheffler, M. Accurate Molecular van der Waals Interactions from Ground-State Electron Density and Free-Atom Reference Data. *Phys. Rev. Lett.* **2009**, *102*, 073005.

152. Tang, H.; Ismail-Beigi, S. First-Principles Study of Boron Sheets and Nanotubes. *Phys. Rev. B* **2010**, *82*, 115412.

153. Wu, X.; Dai, j.; Zhao, Y.; Zhuo, Z.; Yang, J.; Zeng, X. C. Two-Dimensional Boron Monolayer Sheets. *ACS Nano* **2012**, *06*, 7443-7453.

154. Zhai, H. J.; Alexandrova, A. N.; Birch, K. A.; Boldyrev, A. I.; Wang, L. S. Hepta- and Octacoordinate Boron in Molecular Wheels of Eight- and Nine-atom Boron Clusters: Observation and Confirmation. *Angew. Chem. Int. Ed.* **2003**, *42*, 6004-6008.

155. Alexandrova, A. N.; Boldyrev, A. I.; Zhai, H. J.; Wang, L. S. All-boron Aromatic Clusters as Potential New Inorganic Ligands and Building Blocks in Chemistry. Coord. *Chem. Rev.* **2006**, *250*, 2811-2866.

156. Oger, E.; Crawford, N. R. M.; Kelting, R.; Weis, P; Kappes, M.M.; Ahlrichs, R. Boron Cluster Cations: Transition from Planar to Cylindrical Structures. *Angew. Chem. Int. Ed.* **2007**, *46*, 8503-8506.

157. Sergeeva, A. P.; Zubarev, D. Y.; Zhai, H. J.; Boldyrev, A. I.; Wang, L. S. A. Photoelectron Spectroscopic and Theoretical Study of $B_{16}^-$and B_{16}^{2-} An All-Boron Naphthalene. *J. Am. Chem. Soc.* **2008**, *130*, 7244-7246.

158. Sergeeva, A. P.; Averkiev, B. B.; Zhai, H. J.; Boldyrev, A. I.; Wang, L. S. All Boron Analogues of Aromatic Hydrocarbons: B_{17}^- and B_{18}^-. *J. Chem. Phys.* **2011**, *134*, 224304.

159. Huang, W.; Sergeeva, A.P.; Zhai, H-J; Averkiev, B.B.; Wang L-S; Boldyrev, A.I. A Concentric Planar Doubly π-aromatic B_{19}^- Cluster. *Nat. Chem.* **2010**, *2*, 202-206.

160. Piazza, Z. A. et al. A Photoelectron Spectroscopy and *Ab initio* Study of B_{21}^-: Negatively Charged Boron Clusters Continue to be Planar at 21. *J. Chem. Phys.* **2012**, *136*, 104310.

161. Sergeeva, A. P. *et al.* B_{22}^- and B_{23}^-: All-boron Analogues of Anthracene and Phenanthrene. *J. Am. Chem. Soc.* **2012**, *134*, 18065-18073.

162. Popov, I. A., Piazza, Z. A., Li, W. L., Wang, L. S. & Boldyrev, A. I. A Combined Photoelectron Spectroscopy and *Ab initio* Study of the Quasi-planar B_{24}^- Cluster. *J. Chem. Phys.* **2013**, *139*, 144307.

163. Paier, J.; Marsman, M.; Hummer, K.; Kresse, G.; Gerber, C. I.; Angyán, J. G. Screened Hybrid Density Functionals Applied to Solids. *J. Chem. Phys.* **2006**, *124*, 154709.

164. Paier, J.; Marsman, M.; Kresse, G. Why Does the B3LYP Hybrid Functional Fail for Metals? *J. Chem. Phys.* **2007**, *127*, 024103.